Research article

Depth-dependent sulfur speciation in modern carbonate microbialites from a monomictic lake

Jeanne Caumartin[1,2]✉ Karim Benzerara[1]✉ Robin Havas[3] Christophe Thomazo[3,4] Neha Mehta[1,5] Vladimir Betancourt[6] Luis Carlos Colocho Hurtarte[7] Marine Cotte[8,9] Imène Estève[1] Didier Jézéquel[10] Electra Kotopoulou[2,11] Pierre Sans-Jofre[1] Rosaluz Tavera[6] Purificación López-García[2]

[1] Sorbonne Université, Museum National d'Histoire Naturelle, UMR CNRS 7590, Institut de Minéralogie, de Physique des Matériaux et de Cosmochimie (IMPMC), 75005 Paris, France
[2] Unité d'Ecologie Systématique et Evolution, CNRS, Université Paris-Saclay, AgroParisTech, Gif-sur-Yvette, France
[3] Université de Bourgogne Europe, Biogéosciences, UMR CNRS EPHE 6282, Dijon, France
[4] Institut Universitaire de France, Paris, France
[5] Department of Geosciences, Université Libre de Bruxelles, Brussels, Belgium
[6] Departamento de Ecología y Recursos Naturales, Universidad Nacional Autónoma de Mexico, DF Mexico, Mexico
[7] Diamond Light Source Ltd, Harwell Science and Innovation Campus, OX11 0DE Oxfordshire, UK
[8] European Synchrotron Radiation Facility, Beamline ID21, 38000 Grenoble, France
[9] Sorbonne Université, CNRS, Laboratoire d'archeologie moleculaire et structurale, LAMS, 75005 Paris, France
[10] Institut de physique du globe de Paris, CNRS UMR 7154, Université de Paris & UMR CARRTEL, INRAE-USMB, France
[11] Physique des Interactions Ioniques et Moléculaires, Université Aix-Marseille, CNRS, Marseille, France

✉ **Correspondence to:** Karim Benzerara: karim.benzerara@sorbonne-universite.fr or Jeanne Caumartin: jeanne.caumartin@orange.fr

Author contributions: Conceptualization: KB, PL, JC, CT, RH; Funding Acquisition: KB, PL, CT, EK; Investigation: JC, KB, PL, RH, CT, NM, VB, EK, DJ, PS, RT; Methodology: LC, MC, IE; Supervision: KB, PL; Validation: KB, PL, CT, NM, LC, MC, IE; Writing — original draft: JC, KB, PL, CT, RH

Data, code, and outputs: Caumartin and Benzerara (2026): https://doi.org/10.5281/zenodo.20261425

Submitted: 2025-09-10
Accepted: 2026-03-13
Published: 2026-05-18

Production editor:
Mark Torres

Handling editor:
Ernest Chi Fru

Reviews:
Jérémie Aubineau
and one anonymous reviewer

Copyediting:
Yingbo Li,
Marthe Klöcking

Recently, carbonate microbialites were discovered in Lake Alchichica, Mexico, forming below the oxycline (down to 40 m depth), under seasonally anoxic conditions, while conspicuous microbialites also grow at shallower depths under continuously oxic conditions. Here, we investigated sulfur (S) speciation in these microbialites at submicrometer resolution using synchrotron-based X-ray absorption near-edge structure (XANES) spectroscopy, complemented by laboratory X-ray fluorescence (XRF) mapping, scanning electron microscopy (SEM) and energy dispersive X-ray spectrometry (EDXS). Our findings revealed that S is pervasive in both shallow and deep microbialites. However, S speciation varied with depth: while carbonate-associated sulfates (CAS) and organic S compounds were present at all depths, more reduced S species were enriched in the aragonitic layers of deep microbialites, particularly in association with remnants of biogenic structures. These variations in S speciation suggest that deep Alchichica microbialites continue to accrete during seasonal anoxia. Moreover, our results indicate that S speciation in modern microbialites is influenced by ambient redox conditions. By documenting the processes affecting S speciation in a modern microbialitic system, this study provides a framework for future investigations into ancient microbialites that formed under sulfidic conditions.

1 Introduction

Microbialites are organo-sedimentary rocks formed by benthic microbial communities that induce, influence, and/or control mineral precipitation, and/or trap and bind detrital particles (Walter et al., 1980; Burne and Moore, 1987). They are abundant throughout the geological record, from the Archean, the oldest examples representing some of the earliest traces of life (Allwood et al., 2006), to the present, where they still form in diverse aqueous environments (Caumartin et al., 2023). Since microbialites record at least partly the geochemical and biological conditions of their growth, they can serve as valuable archives for reconstructing paleoenvironments (Ollivier et al., 2018; Hohl

and Viehmann, 2021; Antunes et al., 2022). However, to interpret redox conditions from ancient microbialites, we must first explore in modern ones how such changes are encoded within their mineralogy, chemistry and associated microbial biofilms (Pages et al., 2014). Most modern microbialites develop under oxic conditions and are dominated by oxygenic phototrophs such as cyanobacteria. In contrast, microbialites that formed before or shortly after the GOE likely developed under anoxic conditions, possibly involving a greater contribution from anoxygenic phototrophs that use alternative electron donors to O_2 (Bosak et al., 2007; Shih et al., 2016; Visscher et al., 2020). This discrepancy casts doubt on the suitability of modern microbialites forming in oxic environments as analogs for their ancient counterparts formed under anoxic (sulfidic) conditions, particularly when reconstructing redox dynamics from preserved geochemical signals. Modern microbialites forming under anoxic or seasonally anoxic conditions may therefore offer more appropriate analogs.

Lake Alchichica is a monomictic crater lake in Mexico that hosts extensive carbonate microbialites. The lake stratifies seasonally, with an oxycline fluctuating between approximately 20 and 36 m. The hypolimnion becomes anoxic from April to October. Moreover, the lake is characterized by a relatively elevated S concentration, ranging from 10 to 12 mM (Hernández et al., 2014; Muller et al., 2023; Alcocer, 2022). This is particularly interesting since S has been shown to be an important element in the functioning of some microbialites: in addition to being a major element for biomass, S undergoes redox transformations such as sulfate (SO_4^{2-}) reduction that may favor carbonate precipitation (Visscher et al., 2000). In this study, we examined microbialites collected from multiple water depths in the Lake Alchichica, including the 40 m deep samples located below the seasonal oxycline in anoxic waters. These deep microbialites provide a unique opportunity to investigate whether and how anoxic conditions are recorded in their mineral assemblages and S chemistry. In particular, we compare S speciation in deep microbialites with that of their counterparts developing in permanently oxic shallow waters. Our study reveals marked differences in S speciation between these settings, allowing us to discuss some processes influencing S speciation in these modern microbialites.

2 Materials and methods

2.1 Lake Alchichica setting

Lake Alchichica (19°24'49.45"N; 97°24'11.25"W) is a crater lake located within the Neogene-Eocene Trans-Mexican volcanic belt (TMVB), in the Serdán-Oriental Basin of central Mexico, at an elevation of 2326 m (Ferrari et al., 2012; Chako Tchamabé et al., 2020; Zeyen et al., 2021). This oligotrophic, endorheic lake is mainly fed by rainwater and groundwater (Zeyen et al., 2019). Among a series of crater lakes in the region, including Atexcac, Quechulac, La Preciosa, Aljojuca, and Tecuitlapa, Alchichica exhibits the highest alkalinity and salinity (from 1.23 to 43 mM [HCO_3^-], and from 0.1 to 9 psu, respectively), forming part of an alkalinity-salinity gradient across the region (Zeyen et al., 2017). The lake's physicochemical parameters have been monitored since at least 1941, showing that Alchichica is a monomictic lake, undergoing seasonal stratification with a single annual mixing event during winter (Alcocer, 2022). Its water column becomes anoxic below depths of 20–36 m, from April to October (Alcocer, 2022), with an oxic-anoxic transition characterized by a dissolved O_2 concentration varying between 0 and 5 mg L^{-1}. Moreover, Lake Alchichica is well known for hosting modern microbialites that form an extensive carbonate reef along the shoreline.

2.2 Microbialite and water sampling

2.2.1 *Microbialite samples*

Microbialite samples were collected from the northern shore of Lake Alchichica during two field campaigns in May 2019 and October 2022. In 2019, four samples were collected from depths of 5, 10, 20 and 40 m. In 2022, additional samples were collected from five depths: 3, 10, 20, 30 and 40 m. Samples collected in 2022 were registered in the SESAR catalog (https://www.geosamples.org/), a community platform supporting management and sharing of samples in the Earth, Environmental, and Planetary Sciences community. For analyses, a particular focus was applied to samples taken from 10, 30 and 40 m (respectively: AL22_mb_10m, igsn:10.58052/IEMEX10AL22; AL22_mb_30m, igsn:10.58052/IEMEX30AL22, AL22_mb_40m, igsn:10.58052/IEMEX40AL22; see also Caumartin and Benzerara, 2026). The 2019 samples were used to highlight visual differences with the 2022 samples and to complement bulk chemical analyses. While seasonal variations in the water column chemistry are documented, their effects on microbialite chemistry and mineralogy are more difficult to assess since (i) microbialite samples integrate conditions over multiple seasons and (ii) the dataset in the present study is limited for robust seasonal analysis. However, the two sampling campaigns provided some kind of duplicates for microbialite samples, allowing us to assess the impact of depth on microbialite composition. All samples were collected by scuba diving. During the 2022 campaign, the water column was anoxic below 36 m (i.e. dissolved oxygen below a detection limit of 0.01 mg L^{-1}). In 2019, anoxia occurred below 23 m. Shallow microbialites (< 20 m) were mainly composed of carbonates, with a dominant assemblage of hydromagnesite ($Mg_5(CO_3)_4(OH)_2.4H_2O$) and aragonite ($CaCO_3$; Zeyen et al., 2019, 2021). By contrast, deeper microbialites (> 20 m) were composed of hydromagnesite, aragonite, and huntite ($CaMg_3(CO_3)_4$; Caumartin et al., 2025). The biofilms at the surface of the microbialites analyzed here exhibited differences in pigmentation depending on the time and depth of collection. In 2019, the pigmentation ranged from green in the most superficial samples to red-purple in the deepest samples, whereas in 2022 it ranged from green at the surface to red–black in the deepest samples. Previous studies have demonstrated that the prokaryotic communities associated with surface microbialites in Lake

Alchichica are dominated by oxygenic photosynthesizers, together with heterotrophic taxa and a diverse assemblage of anoxygenic phototrophs. In contrast, sulfate-reducing microorganisms appear to be present in relatively low abundance (Saghaï et al., 2015; Iniesto et al., 2021; Caumartin and Benzerara, 2026).

2.2.2 Water samples

Water column samples were collected during the same two campaigns in May 2019 and October 2022. Samples were collected using a Niskin bottle from a boat anchored near the lake's center (Caumartin and Benzerara, 2026). In situ measurements of temperature (± 0.01 °C), pH (± 0.1 pH unit), dissolved O_2 (± 0.1 mg L^{-1}) and conductivity (± 0.001 mS cm^{-1}) were taken along depth profiles using a YSI Exo2 multiparameter probe (with automatic temperature and salinity corrections). Water collection depths were determined by labels placed every meter on the sampling rope and these measurements were verified using the depth gauge of a dive watch attached to the Niskin bottle. A total of 24 water samples (including duplicates) were collected at different depths between 0 and 60 m. They were filtered within a few hours after collection using 0.2 µm polyethersulfone (PES) filters and stored in sterile tubes for chemical analyses. For each depth, 6 mL of filtered water were acidified with 2 % nitric acid for ICP-AES analyses. The remaining unacidified water was used for major anion analyses by ion chromatography. Additionally, 12 mL Exetainer tubes were filled with filtered solutions for dissolved inorganic carbon (DIC) measurements.

To better assess seasonal variations in oxygenation within Lake Alchichica, dissolved oxygen concentration data spanning from 1980 to the present were compiled from the literature for a more statistically representative dataset.

2.3 Methods

2.3.1 Water chemistry

Water samples from both campaigns were analyzed at the Institut de Physique du Globe de Paris, France (Caumartin and Benzerara, 2026). Concentrations of major and trace elements (Na, K, Ca, Mg, Fe) and total S were determined using inductively coupled plasma atomic emission spectrometry (ICP-AES). The concentration of Cl was measured using ion chromatography. DIC measurements for both 2019 and 2022 samples were performed using an analytical Precision 2003 gas chromatography isotope-ratio mass spectrometry (GC-IRMS), following the protocol described by Assayag et al. (2006).

2.3.2 Bulk chemical analyses of microbialites

Between 1.5 and 2 g of each microbialite sample was crushed and powdered in an agate mortar. Major and trace element compositions (Caumartin and Benzerara, 2026) were measured by the Service d'Analyse des Roches et Minéraux (SARM, Centre de Recherches Pétrographiques et Géochimiques, Nancy, France). Major element concentrations were determined using an ICP-AES ICap 6500 (Thermo Fischer) after alkali fusion of the rock samples with $LiBO_2$ and subsequent dissolution in HNO_3. Measurement uncertainties ranged between 2 and 25 % for major elements and between 5 and 20 % for trace elements, depending on concentrations (Caumartin and Benzerara, 2026). Organic carbon was measured after full decarbonation, using a carbon-S elemental analyzer (HORIBA EMIA320V2). Total carbon and S analyses were also performed on a second, non-decarbonated aliquot, using the same analyzer.

2.3.3 Preparation of thin and thick sections

Three microbialites sampled at 10, 30, and 40 m depth in October 2022 were impregnated with Araldite resin and cut into 30 µm thick petrographic thin sections by the Bourgogne Lithologie service (Dijon, France). In parallel, slabs from the same three microbialite samples without resin impregnation were cut and polished using a mechanical polisher (EM TXP). Polishing was performed with abrasive pastes of 15.3, 9, 3, 2 and 0.5 µm under a stream of milli-Q water. These resulting 5–7 mm thick polished sections were cleaned in ultrasonic milli-Q water baths.

2.3.4 Scanning electron microscopy and energy-dispersive X-ray spectrometry (SEM-EDXS)

The three thick, non-resin-embedded sections were mounted on aluminum SEM stubs using double-sided carbon tape and carbon-coated. SEM and EDXS analyses (Caumartin and Benzerara, 2026) were conducted using a Zeiss Ultra 55 field emission gun SEM at IMPMC (France). Backscattered electron (BSE) images were obtained using an accelerating voltage of 15 keV, a working distance of ~7.5 mm and an aperture of 60 µm, in the high current mode and an angle selective backscattered (AsB) detector. A Bruker EDS QUANTAX detector was used to determine the elemental compositions of selected areas by energy-dispersive X-ray spectrometry (EDXS). The EDXS elemental maps were semi-quantified using the ESPRIT software (Bruker, 2.5.0.175 version) with the Pb-ZAF method (Pouchou and Pichoir, 1991).

2.3.5 Laboratory X-ray fluorescence spectroscopy (XRF)

Elemental maps of major and trace elements were acquired on thin sections of the microbialites (10, 30 and 40 m depths) using a Bruker M4 Tornado XRF spectrometer at the Laboratoire Géosciences Océan (Brest, France). Measurements were conducted with an X-ray excitation energy of 50 keV and a current of 600 µA, under a 20 mbar vacuum. Scans were performed with a 20 µm spot size over a ~4 x 3 cm^2 area. Each scan (2000 x 1500 pixels) took over 4 hours per sample with a 5 ms dwell time per pixel.

2.3.6 SR-micro X-ray fluorescence mapping (SR-µXRF) and micro X-ray absorption near-edge structure (µ-XANES) spectroscopy at the S K-edge

µXANES and SR-µXRF measurements (Caumartin and Benzerara, 2026) were conducted at the ID21 beamline of the European Synchrotron Radiation Facility (ESRF, Grenoble, France) on microbialites from the 10, 30 and 40 m depths. The scanning X-ray microscope operated under a

vacuum of 10^{-6} bar. The X-ray beam was monochromatized using a Si(111) crystal monochromator, with a beam size of 0.67 µm x 0.44 µm and a photon flux of approximately 10^9–10^{10} photons s^{-1}. The µXRF maps were acquired using an incident beam of ~2.5 keV. XRF spectra were recorded using a silicon drift diode (SDD) detector with a dwell time of 0.1–0.2 s, without any attenuator. The scanned areas measured between 25 µm x 60 µm and 500 µm x 500 µm with a scanning step between 0.4 and 4 µm/pixel. Moreover, the incident X-ray beam energy was tuned over a range of 2.46–2.53 keV, in increments of 0.25 eV, to measure µXANES spectra at the S K-edge. Energy calibration was performed using the white line of a gypsum ($CaSO_4$) standard at 2.482 keV. Speciation maps were obtained by the collection of hyperspectral µXRF maps at 60 energies (from 2.46 to 2.47 keV with steps of 2 eV, 2.4705 to 2.486 keV with steps of 0.5 eV and from 2.486 to 2.53 keV with steps of 2 eV).

2.3.7 µXANES and SR-µXRF data processing

S K-edge µXANES spectra were analyzed using the Athena software (0.9.26 version). All spectra were aligned to the gypsum white line at 2.482 keV. The edge jump of each spectrum was normalized to 1 after fitting the baseline of the pre-edge at zero. Two approaches were followed for XANES fitting. First, spectra were fitted using a linear combination of reference spectra. Second, spectra were modelled by spectrum deconvolution using peak fitting. Two arctangent step functions were applied to fit the edge jumps, following the method described by Einsiedl et al. (2007). Each peak was fitted with a Pseudo-Voigt function (Wiltfong et al., 2005; Vogt et al., 2023), with one or two pseudo-Voigts used to accurately fit the SO_4^{2-} peak. For this method, peak centers corresponding to the characteristic energies of specific S oxidation states, were initially identified visually to guide the iterations of the Levenberg-Marquardt model used by the Athena software until convergence. As the Levenberg-Marquardt procedure involves non-linear least-squares minimization and since the available data do not support precise uncertainty estimation, Athena software applies a default uncertainty of 1 (see Athena 0.9.26 documentation), resulting in notably low X^2 values. Therefore, fit quality was evaluated comparatively relying on R-factor and reduced X^2 statistical metrics as guidelines, with successive improvements in the reduced X^2. If the initial fit failed to converge, an additional peak was introduced to represent a distinct spectral component. This inclusion was considered valid when it led to a substantial reduction in the reduced X^2, mostly by at least a factor of two, thereby enhancing the model without overfitting. Overall, this fitting strategy allowed us to assess relative spectral variations between microbialites associated with variations of the relative contributions from the different S species.

The SR-XRF maps were batch-fitted using the PyMca software (5.9.2 version; Solé et al., 2007) in order to obtain S and phosphorus elemental maps. Intensity distributions (histograms) of the elemental maps were extracted using the ImageJ software (1.54q version). Hyperspectral maps were also fitted, aligned and cropped using PyMca software. The hyperspectral map presented in this study was analyzed using the k-means clustering method on Quasar software from the Orange environment (version 1.9.2; Toplak et al., 2021, Orange Website: https://orangedatamining.com/). The k-means clustering method is a multivariate technique for iteratively finding clusters in a data set. It alternates between two steps after defining a number of initial centroids for clusters: (i) it identifies for each centroid the subset of points that is closer to it than to any other center, and (ii) calculates a vector of the mean of each feature for the data points in each cluster, which becomes the new center of the cluster (Hastie et al., 2009).

3 Results

3.1 Water column

The mean annual temperature of Lake Alchichica's water column is ~16 °C (Alcocer, 2022). The bulk chemistry of the lake's water column at varying depths has been well documented since at least 1998 (Alcocer and Lugo, 2003; Kaźmierczak et al., 2011; Bautista-Reyes and Macek, 2012; Valdespino-Castillo et al., 2014; Sánchez Medina et al., 2016; Zeyen et al., 2021; Alcántara-Hernández et al., 2022; Alcocer, 2022; Vilaclara et al., 2022; Havas et al., 2023; Muller et al., 2023; Caumartin et al., 2025). In particular, records of dissolved O_2 concentrations show that Lake Alchichica's water column undergoes seasonal stratification each year, typically between April and October, with anoxic conditions developing below depths ranging from 20 to 30 m (Fig. 1). This seasonal anoxia has been consistently observed since 1998 (Fig. 1).

Consistent with this pattern, Lake Alchichica's water column was anoxic at a depth of 40 m, where microbialites were sampled during both the May 2019 (early stratification period) and October 2022 (late stratification period) field campaigns (Fig. S1 in the Supplementary Material). The concentrations of major cations and anions were measured during the same periods (Caumartin and Benzerara, 2026). The pH of the water was ~9.2 ± 0.1 throughout the entire water column for both collection times. DIC concentrations were high, averaging 36 ± 0.05 mM in 2022. Measured concentrations of dissolved Mg and Ca were 18.10 ± 0.26 mM and 0.220 ± 0.005 mM, respectively. Overall, the water column was supersaturated with respect to calcium and magnesium carbonate phases, including aragonite, hydromagnesite and huntite, at all depths (Zeyen et al., 2021).

Additionally, dissolved S and iron concentrations were measured by ICP-AES throughout the water column in both May 2019 and October 2022 (Fig. S1). Both elements displayed relatively stable concentrations across depths, with mean values of 10.35 ± 0.52 mM for S and 0.72 ± 0.04 µM for Fe. A slight decrease in concentration was observed below the oxycline during both field campaigns. In 2022, localized variations in iron were detected, including a peak at 7.42 ± 0.37 µM just above the oxycline. Although sulfide concentrations were not directly measured, an odor of H_2S

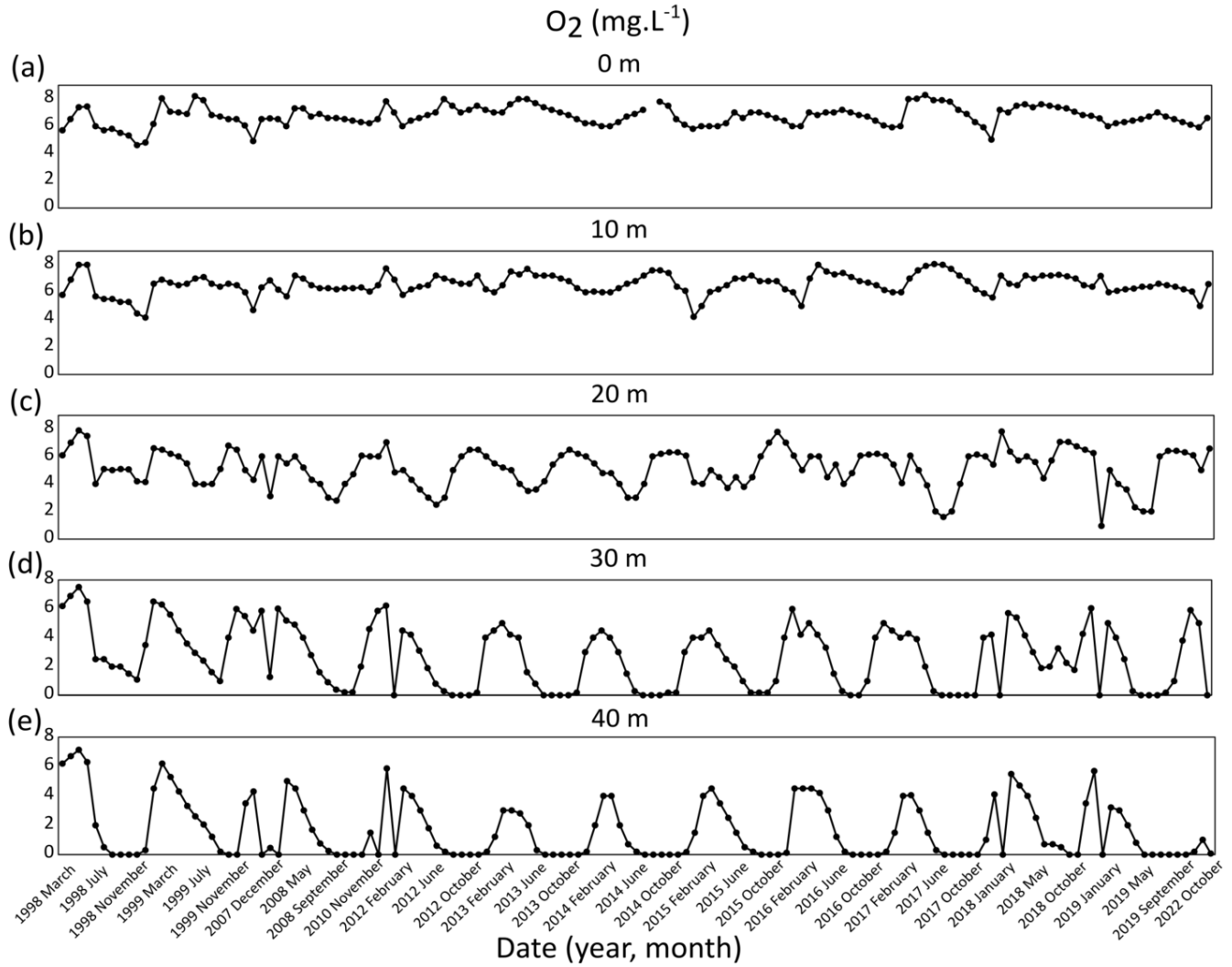

Figure 1. Variations in O_2 concentration (mg L^{-1}) in the water column of Lake Alchichica from 1998 to 2022. Data are shown for five different depths: 0 m (a), 10 m (b), 20 m (c), 30 m (d) and 40 m (e). Data are sourced from Alcocer and Lugo (2003); Kaźmierczak et al. (2011); Bautista-Reyes and Macek (2012); Valdespino-Castillo et al. (2014); Sánchez Medina et al. (2016); Alcántara-Hernández et al. (2022); Vilaclara et al. (2022) and in situ measurements from this study (2019 and 2022).

in water samples collected below 30 m depth in 2022 was detected, suggesting sulfidic conditions.

3.2 Bulk chemistry and mineralogical analyses of microbialites

The three microbialites analyzed in this study were collected in 2022 from distinct depths: 10 m (permanently oxic water column), 30 m (near the oxycline) and 40 m (seasonally anoxic water column; Fig. 2). These samples displayed marked differences in surface color, both in comparison to one another and relative to samples collected in May 2019 (Havas et al., 2025). The shallowest sample, from 10 m, exhibited a green color (Fig. 2). In contrast, the 30 m deep sample had a dark red surface and the deepest sample, at 40 m, featured a black surface that turned light grey upon air exposure and was also covered by a thin red surficial biofilm layer (Fig. 2). The mineralogical composition of the samples was previously determined using XRD and FTIR spectroscopy (Caumartin et al., 2025). These analyses showed that the 10 m deep sample was composed of aragonite and hydromagnesite, while both the 30 m and 40 m deep samples consisted of a mixed aragonite-hydromagnesite-huntite mineral assemblage (Fig. S2a-c). Interestingly, no clear correlation was detected between the sampling depth and the bulk chemical composition of the microbialites (Fig. S2d). S was detected in all samples by bulk analyses, though at low concentrations, averaging 0.035 ± 0.002 wt% (Fig. 3). Similarly, the organic carbon content was uniformly low across all depths, with an average of 0.17 ± 0.008 wt% (Caumartin and Benzerara, 2026).

3.3 Laboratory-based XRF analyses of microbialite thin sections

Thin sections of the three microbialite samples collected at 10, 30 and 40 m depth in 2022 were scanned using laboratory-based XRF to assess the spatial distribution of S (Fig. 3). The XRF results confirmed the presence of S detected by bulk analyses. Moreover, the elemental

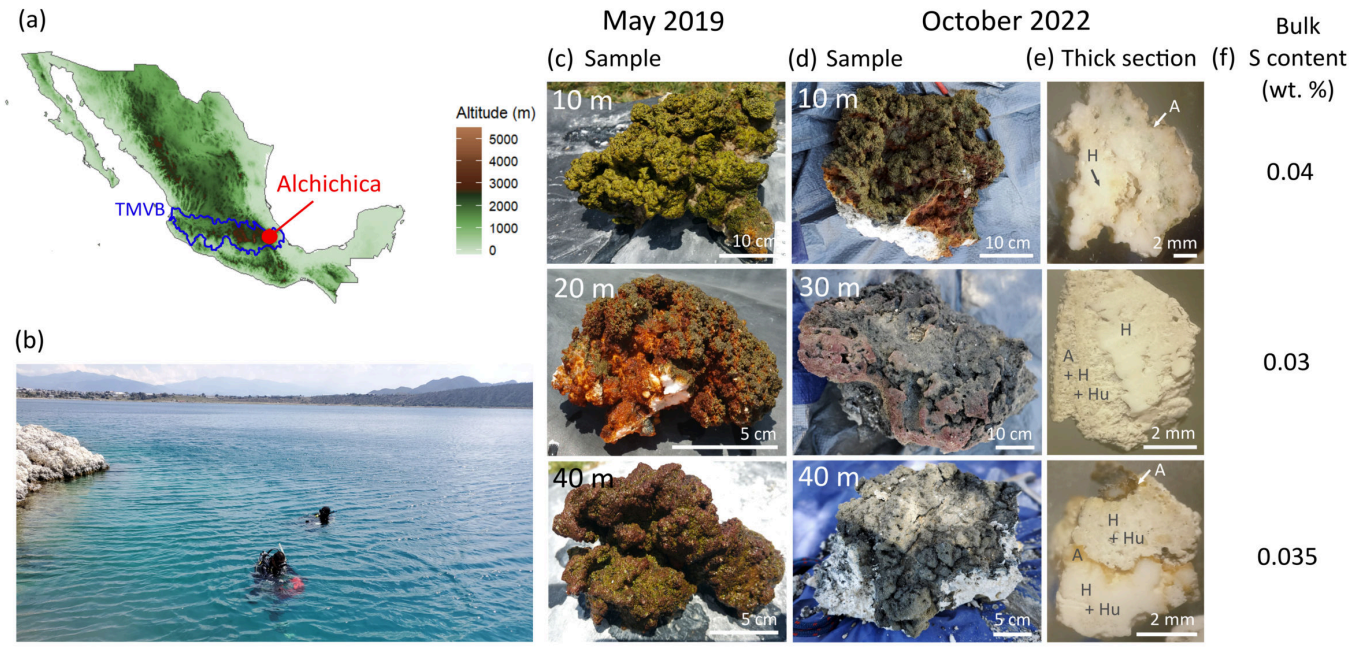

Figure 2. Overview of the Lake Alchichica locality and general appearance of the microbialite samples. (a) Map of Mexico showing the location of Lake Alchichica within the TMVB (Datasource: Natural Earth and SRTM, Rstudio); (b) Photograph of the microbialite sampling site in Lake Alchichica (October 2022); (c) Depth-dependent morphological variations in microbialites. From top to bottom: Photographs of microbialites collected from 10 m to 40 m depth during early stratification (May 2019); (d) Top to bottom: Photographs of microbialites collected from 10 m to 40 m depths during late stratification (October 2022); (e) From top to bottom: thick section photographs of microbialites from 10 to 40 m depth (October 2022) as shown in (d). The 10 m sample displays two main phases: aragonite (A) on the outer edges and hydromagnesite (H) in the interior. The 30 m sample exhibits a heterogeneous mix of hydromagnesite, aragonite and huntite (Hu). The 40 m sample shows aragonite on the microbialite edges, an oxidized Fe-rich lamina in the central zone, and a mix of hydromagnesite and huntite throughout the rest of the section; (e) Bulk S content (wt% ± 5 %) in microbialites collected from 10 m to 40 m depth (October 2022).

maps revealed that S was preferentially concentrated along the outer rims of the microbialites, in spatial correlation with aragonite. By contrast, the S signal was weaker in hydromagnesite, which composed the bulk mass of the microbialites. Last, S appeared to be more widespread throughout the structure of the deep microbialites (30 and 40 m depths) compared to the shallow ones, even if it globally followed the same pattern with a S enrichment in the aragonite-rich peripheral zones.

3.4 S distribution assessed by SEM-EDXS and SR-μXRF analyses

Representative areas of the 10 m and 40 m deep microbialite thick sections, measuring 0.35 mm x 0.27 mm and 2.65 mm x 1.95 mm, respectively, were mapped semi-quantitatively using SEM-EDXS (Fig. 4). These results are consistent with laboratory-based XRF findings, confirming both (i) the presence of S within the microbialites, with a semi-quantified S content of 0.22 wt%, and (ii) preferential localization of S in aragonite-rich outer rim zones. In the 40 m deep sample, S was not only concentrated in aragonitic areas but was also relatively widespread in association with the huntite phase. Moreover, the S-enriched areas contained remnants of biological structures encrusted by aragonite, as observed in both the shallow and deep samples (Fig. 4c-d).

We also looked for additional S-bearing mineral phases within the microbialites (Fig. 5, Fig. S3). Iron sulfides were detected in the 30 m deep sample (Fig. 5a), with some occurrences also observed in the 40 m deep sample. These iron sulfides appeared as aggregates of euhedral crystals, ~ 1 μm in size, consistent with FeS_2 (Fig. 5b). Occasionally, S was associated with both iron and silicon (Fig. 5c).

To further refine the S distribution within the microbialites, synchrotron-based SR-μXRF imaging was performed on selected regions of thin sections from the 10, 30, and 40 m deep samples collected in 2022. This technique provides sub-micrometer spatial resolution and significantly lower detection limits compared to laboratory-based methods (SEM-EDXS and laboratory-based XRF). A total of 14 maps were acquired: 6 for the 10 m deep sample, 2 for the 30 m deep sample, and 6 for the 40 m deep sample (Fig. S4). Each region of interest corresponding to an SR-μXRF map was subsequently reanalyzed by SEM-EDXS to ensure consistency. These analyses revealed two distinct S distribution patterns: (i) diffuse and (ii) in the form of localized hotspots (Fig. 6). Correlated SR-μXRF and SEM-EDXS maps indicated that all S (diffuse or localized) was preferentially associated with

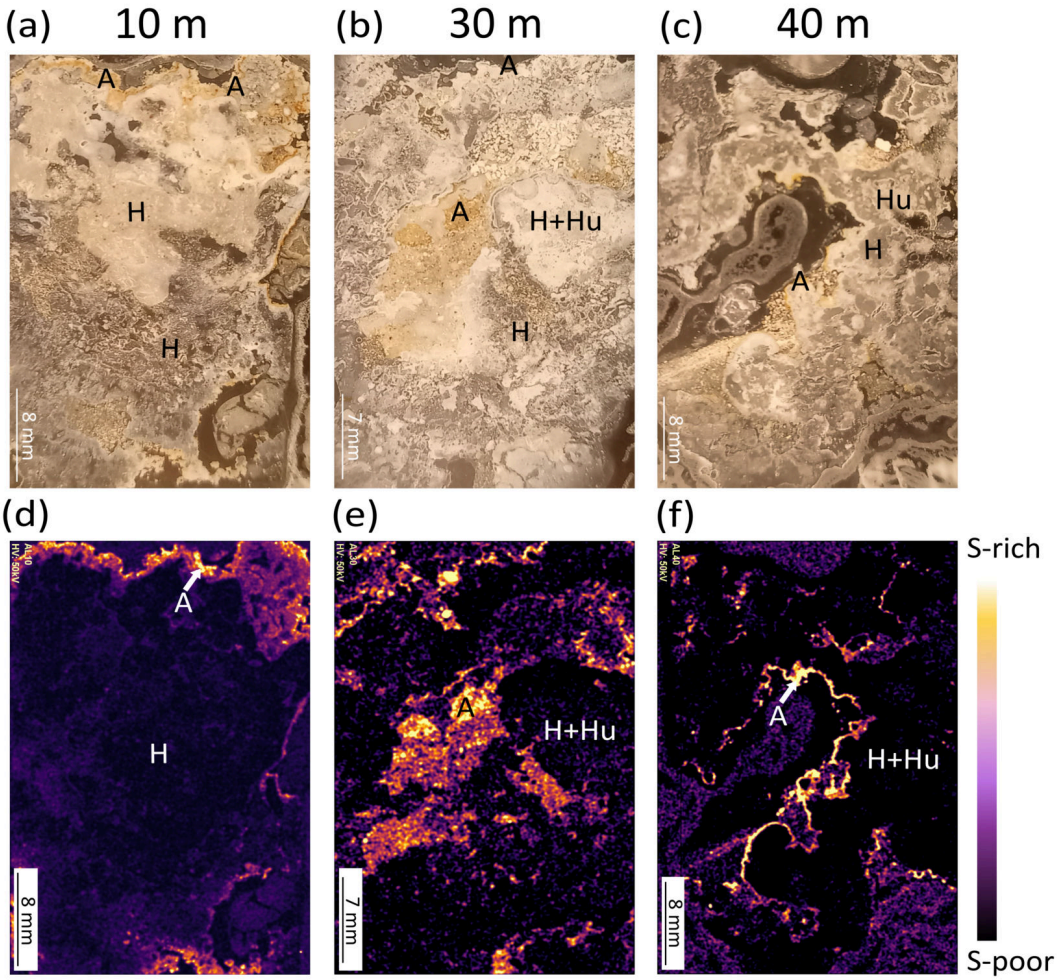

Figure 3. Optical microscopy and laboratory XRF S mapping of Lake Alchichica microbialites thin sections (October 2022). Mineral phases are abbreviated as follows: A = aragonite, H = hydromagnesite, Hu = huntite; (a) Thin section image of the 10 m microbialite sample, showing aragonite concentrated at the outer edge of the microbialite and a core primarily composed of hydromagnesite. (b) Thin section of the 30 m sample, where patches of aragonite are localized within a mixed hydromagnesite-huntite matrix. (c) Thin section of the 40 m sample, with aragonite at the outer edges of the microbialite, hydromagnesite as the main internal phase and localized huntite patches; (d) Laboratory-XRF S map of the 10 m sample, showing a small amount of S along the aragonite-rich outer rim; (e) Laboratory-XRF S map of the 30 m sample, showing S co-localized with aragonite, and to a lesser extent, dispersed in hydromagnesite; (f) Laboratory-XRF S map of the 40 m sample, showing a pronounced S signal along the outer edge of the microbialite and a diffuse signal within the microbialite interior.

aragonite-enriched regions at all sampled depths (Fig. 6). These aragonite-enriched regions were located along the outer rims of the microbialites and commonly contained remnants of encrusted biological structures (Fig. 4).

3.5 S speciation assessed by SR-μXANES

3.5.1 Depth-dependent variations in S redox states within microbialites

To assess S speciation in microbialite samples, μXANES spectra were acquired at the S K-edge, with a total of 28 spectra for the 10 m deep sample, 37 for the 30 m deep sample, and 23 for the 40 m deep sample from 2022 (average spectra of samples from each depth are shown in Fig. 7; all spectra are available in Fig. S5). The spectra display peaks in six distinct energy ranges, associated with different ranges of S oxidation states and/or species (Fig. 7). Peaks were assigned to different S functional groups by comparison with reference spectra and based on Sarret et al. (1999), Myneni (2000), Prietzel et al. (2009), Orthous-Daunay et al. (2010), and on the ID21 database (references for gypsum, native S, pyrite, Na-tetrathionate; Fig. S6), who showed that the energy position of the white line (i.e. the sharpest and most intense absorption peak in the XANES spectrum) increases with the formal oxidation state of S. (i) Peaks in the 2481.9–2482.1 eV energy range were attributed to SO_4^{2-} S(VI); (ii) peaks in the 2479.8–2480.5 eV energy range were assigned to sulfones, sulfonates, or related mixed-valence compounds, consistent with S(IV) to S(V); (iii) peaks in the energy range between 2476.0 and 2478.1 eV were attributed to intermediate-valence S species such as sulfoxides, consistent with S(II), and including possible contributions from mixed-valence compounds; (iv) peaks

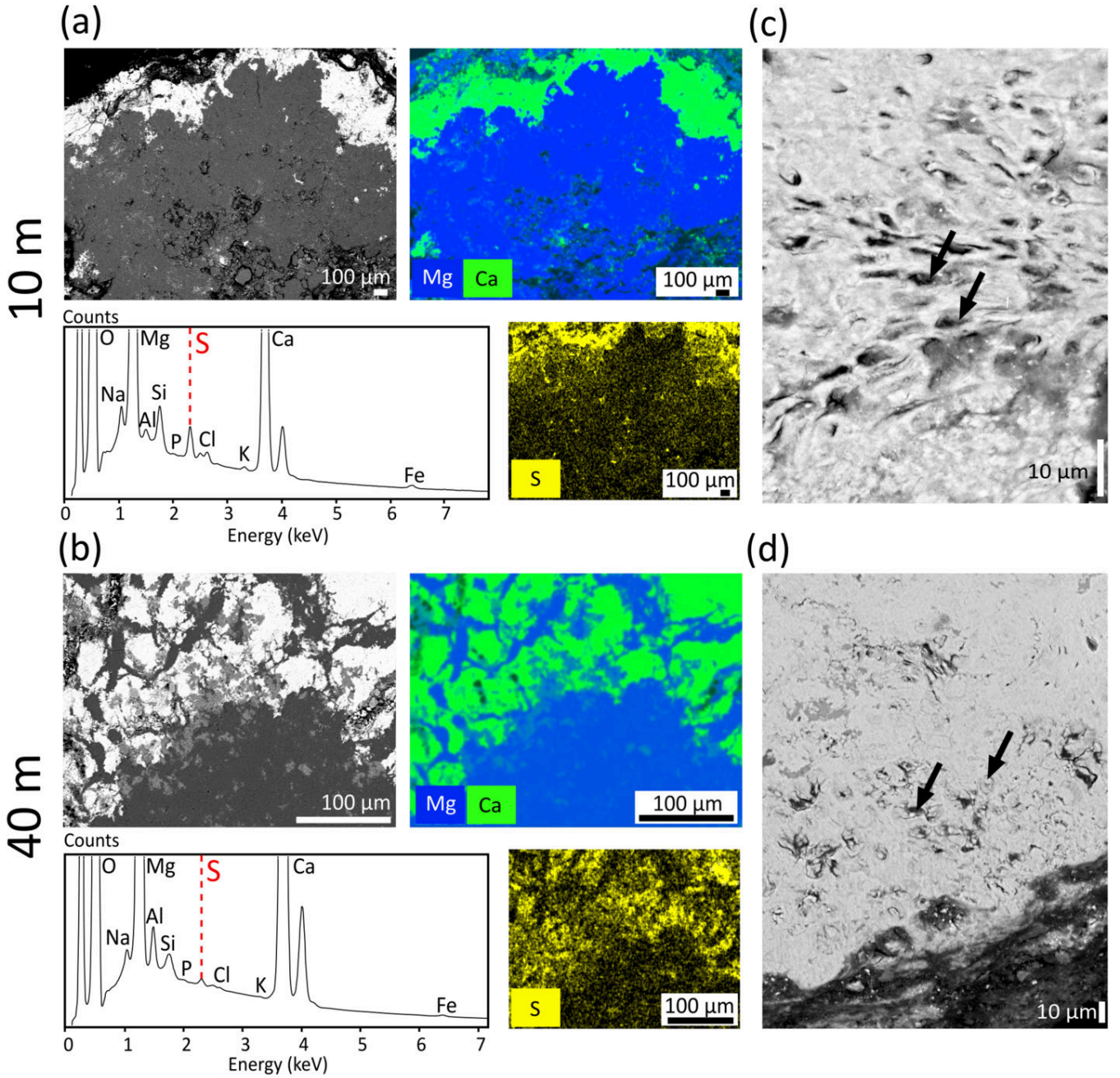

Figure 4. SEM-EDXS detection of S in Lake Alchichica microbialites (October 2022). (a) Top left: SEM image in the BSE mode of the 10 m deep microbialite thin section, showing an aragonitic outer rim (bright) and a deeper part composed of hydromagnesite (dark grey). Top right: EDXS elemental map showing magnesium and calcium distribution, distinguishing aragonite along the outer rim and hydromagnesite. Bottom left: EDXS spectrum from the imaged area shown above. The S peak is detected at 2.307 keV. Bottom right: EDXS S map in the same zone, illustrating S enrichment along the aragonite-rich outer rim of the microbialite; (b) Top left: SEM BSE image of the 40 m deep microbialite thin section, showing a fractured aragonite layer (bright white) overlaying a hydromagnesite-rich core (dark grey). Huntite patches appear at the aragonite-hydromagnesite interfaces (light grey). Top right: EDXS magnesium and calcium maps for the same zone, showing the distribution of hydromagnesite and aragonite at the outer rim. Bottom left: EDXS spectrum of the area, with S detected at 2.307 keV. Bottom right: EDXS S map for the same zone, indicating S enrichment along the outer rim of the microbialite. (c) SEM-BSE image of an aragonitic surface layer from the 10 m deep sample. Aragonite appears in white, while hydromagnesite appears in dark grey. Arrows indicate rounded objects interpreted as biogenic structures encrusted by aragonite following Couradeau et al. (2013) and Saghaï et al. (2015). (d) SEM-BSE image of an aragonitic layer at the surface of the 40 m deep sample. Aragonite appears in white. Arrows indicate rounded object interpreted as encrusted microbial cells, typical textures observed in the aragonitic layer rich in S.

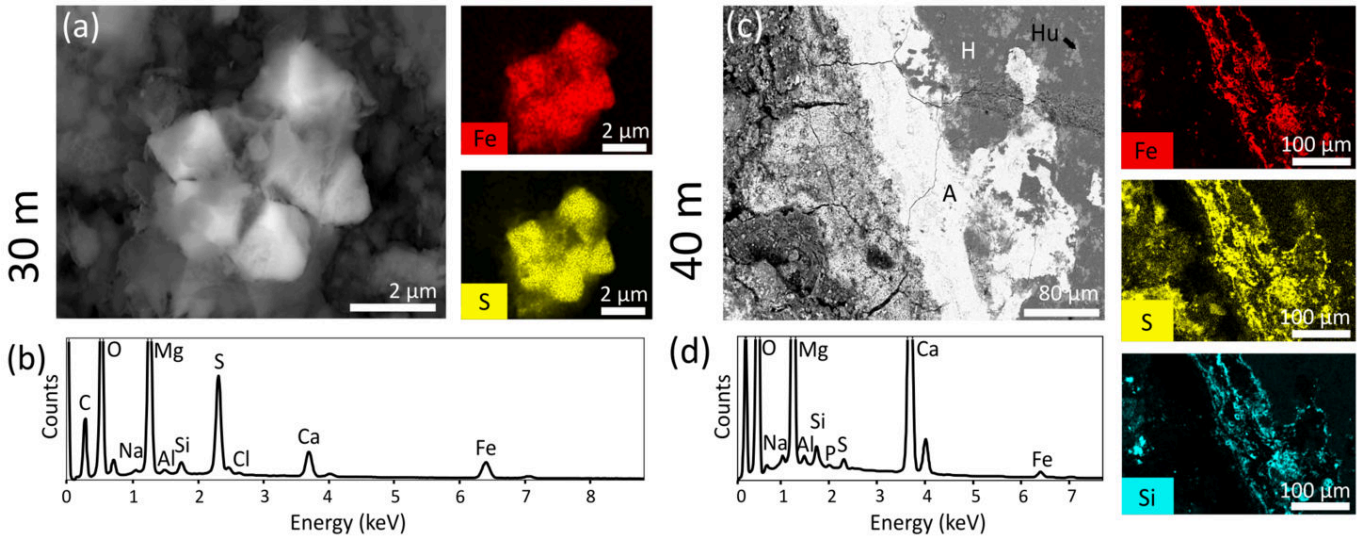

Figure 5. SEM-EDXS detection of S-bearing mineral phases in Lake Alchichica deep microbialites (October 2022). (a) SEM-BSE image of a ~1 µm euhedral crystal aggregate in a 30 m deep microbialite with associated EDXS elemental maps of iron and S on the same area; (b) EDXS spectrum of the same area as in (a), highlighting the detection of S and iron; (c) SEM-BSE image of an aragonitic zone (white) surrounded by hydromagnesite-huntite in a 40 m deep microbialite with associated EDXS elemental maps of iron, S and silicon, showing laminae within the aragonitic layer; (d) EDXS spectrum of the area shown in (c), indicating the detection of silicon, S and iron.

in the 2472.9–2473.9 eV energy range were interpreted as originating from some organic S compounds with closely overlapping peak positions, making individual species difficult to distinguish. These compounds included amino acid- and aryl disulfides, heterocyclic S such as thiophene, and polysulfides, consistent with S oxidation states from -I to 0.5; (v) peaks in the 2472.5–2472.9 eV energy range were attributed to S^0 (elemental S); finally, (vi) peaks in the 2471–2472.2 eV energy range were attributed to S(-I), i.e. disulfides in FeS_2. The absence of spectral features below 2471 eV ruled out the presence of more reduced inorganic sulfide species. Interestingly, an overview of all K-edge spectra revealed a more pronounced spectral contribution of reduced S species at greater depths (Fig. 7, Fig. S5). Notably, several spectra from the 40 m deep microbialite displayed particularly intense peaks at 2472.1 eV and 2477.7 eV, which were less pronounced or absent in the shallower 30 and 10 m deep samples (Fig. 7).

The combined SR-µXRF and µXANES analyses showed that reduced S species were predominantly localized within S hotspots, while diffuse S regions mostly contained SO_4^{2-} (Fig. 7). Notably, SO_4^{2-}species were detected in all spectra, regardless of whether they originated from diffuse regions or hotspots, and across all microbialite depths (Fig. 7, Fig. S5). Linear combination fitting was applied to the µXANES spectra to better constrain the S species present in the microbialites. Reference compounds from the ID21 database, along with an internal SO_4^{2-}standard (i.e. a spectrum showing SO_4^{2-} only and measured on one spot in the 30 m deep microbialite, see Fig. S5) were used for fitting (Figs S5, S6). Among the most conclusive fits for reduced S species, FeS_2 was identified in both the 30 and 40 m deep samples, consistent with SEM observations (Fig. 8a-c). In the 10 m deep microbialite, while the S^0 reference adequately explained the peak at ~2472.5 eV, the internal SO_4^{2-} standard was not sufficient to fully fit the other spectral features (Fig. 8d). Similarly, in the deepest 40 m sample, the prominent peaks corresponding to reduced species (at ~2472.3 eV, ~2477.7 eV) could not be fully fitted with available reference spectra. The closest fits were achieved by combining S^0 with S(IV) (we used Na-tetrathionate as a reference compound to model species with notably a peak at 2477.7 eV; Fig. 8a). Overall, this approach supported the identification of FeS_2 and additional S-bearing phases in the Alchichica microbialites, but it did not fully account for the statistical variability in S speciation across samples. Therefore, we used an alternative approach.

To better assess depth-related variations in S speciation, spectral deconvolution of the XANES data was performed. In this approach, each spectrum was modeled using two arctangent functions to represent the edge jumps, along with four to seven pseudo-Voigt functions to fit individual absorption peaks. Each peak center was assigned to a specific oxidation state of S based on the energy range where it lies, and the peak fitting algorithm was iterated until convergence by minimizing both the R-factor and X^2 values (see Methods Section 2.3.7, Fig. S7). While not providing absolute proportions of distinct S species, this allows for a reliable description of their relative variations with depth. The spectral variations were estimated from changes in the relative areas of the fitted pseudo-Voigt components (Fig. 9). The deconvolution revealed that S(VI) species largely dominated the XANES signal in both the 10 and 30 m deep microbialites, although minor signals of reduced species were present in some spectra acquired from the 10 m deep microbialite and in all but three spectra from the 30 m deep microbialites. In contrast, the relative contribution of reduced S such as sulfides, S^0, organic polysulfides, and

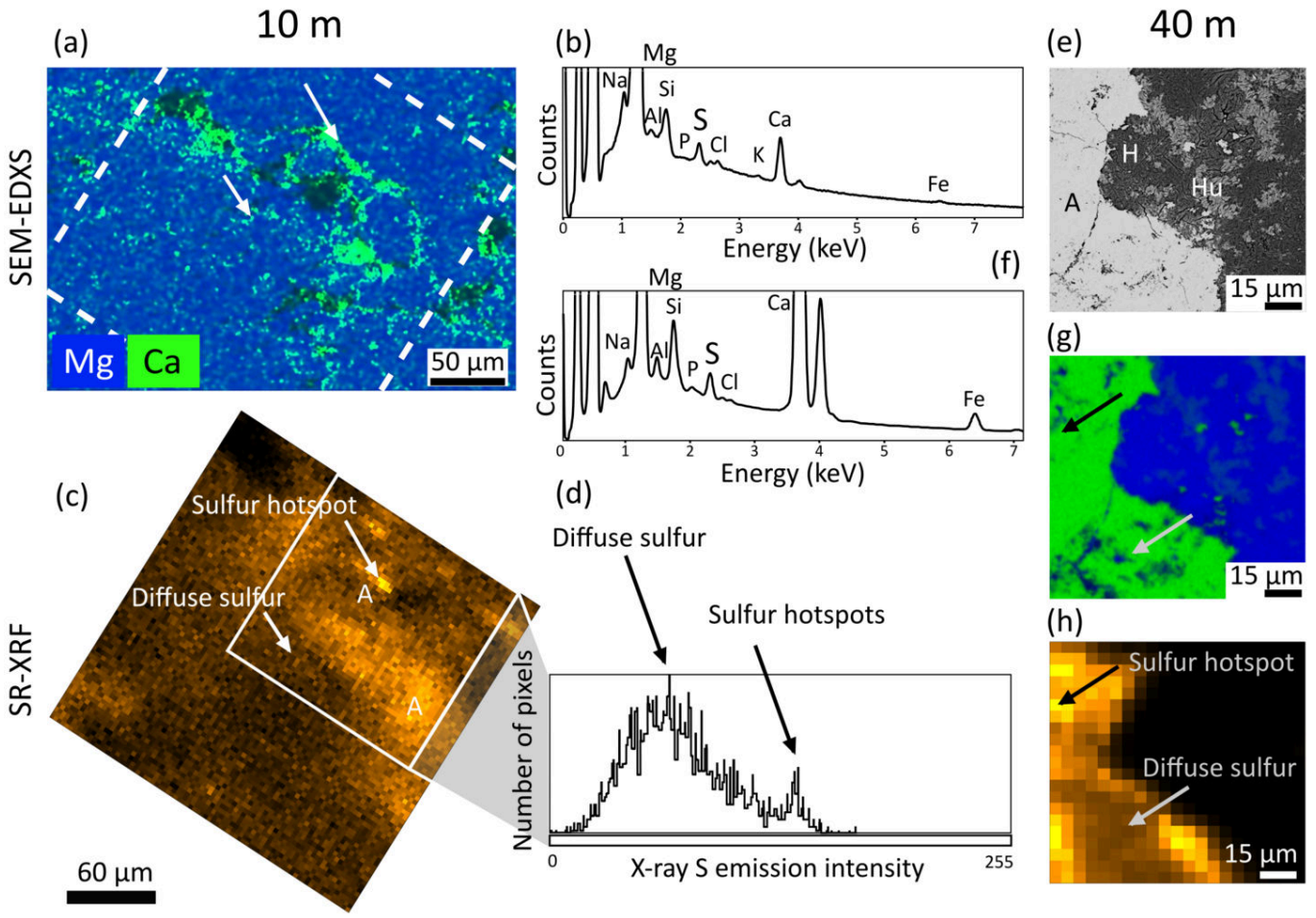

Figure 6. Correlative SEM-EDXS and SR-µXRF analyses of S distribution in Lake Alchichica 10 and 40 m deep microbialites (30 m shown in Fig. S4). (a) SEM-EDXS elemental map of magnesium (blue) and calcium (green) of a hydromagnesite-aragonite zone in the 10 m deep microbialite sample. The dashed white square indicates the area over which an EDXS spectrum and an SR-µXRF S map were acquired. The white arrows correspond to the examples of diffuse S and S hotspot shown in (c); (b) Average EDXS spectrum corresponding to the area depicted by a white square in (a), highlighting the detection of S; (c) SR-µXRF S map of the same area as that observed by SEM in image (a). The arrows indicate one S hotspot and one diffuse S area; (d) Histogram of S XRF signal intensity over the area boxed in (c). The distribution shows a bimodal distribution: the larger, broader and low-intensity peak covers a wide range of intensity under ~130 and is associated with diffuse S and the second, narrower and higher-intensity one ranging from ~130 to ~200 is associated with S hotspots; (e) SEM BSE image of an aragonite-hydromagnesite-huntite interface near the outer rim of the 40 m deep microbialite sample; (f) EDXS spectrum from (e), showing the detection of S; (g) EDXS elemental map of magnesium (blue) and calcium (green) corresponding to (e). The arrows correspond to the examples of diffuse and hotspot S shown in (h); (h) SR-XRF S map of the same area. The arrows indicate one S hotspot and one diffuse S area.

S(II) species to the spectral signal increased dramatically by ~4.5-fold on average in the 40 m deep microbialite, despite some spatial heterogeneity (Fig. 9).

3.5.2 *Reduced S hotspots associated with aragonite-encrusted biogenic structures*

In order to better locate the different S species, we acquired an SR-µXANES hyperspectral map of an aragonitic layer from the 40 m deep microbialite, generating one XANES spectrum per pixel (Fig. 10a). Based on the average XANES spectrum across the scanned area, two spectral regions of interest spanning the 2471–2481.9 and 2481.9–2483 eV energy ranges were selected, corresponding to (i) a large panel of reduced S species, and (ii) oxidized S(VI), respectively (Fig. 10d). Emission maps derived from these ranges revealed that S species, in particular all reduced S species, were concentrated in S hotspots, measuring approximately three to six micrometers in width (Fig. 10c). A k-means clustering method was further applied to the spectra from each pixel of the hyperspectral map. This approach enabled the identification of four clusters with distinct spectral features, primarily differing in relative intensity. In particular, the hotspots displayed an average spectrum with three peaks: (i) the main one at 2482.1 eV, corresponding to S(VI), (ii) one at 2472.2 eV and (iii) a smaller one at 2477.7 eV. The latter two peaks were ~2.5-fold and ~3.5-fold more intense, respectively, in the hotspots compared to the average spectrum of the entire scanned area (based on normalized peak height ratios in

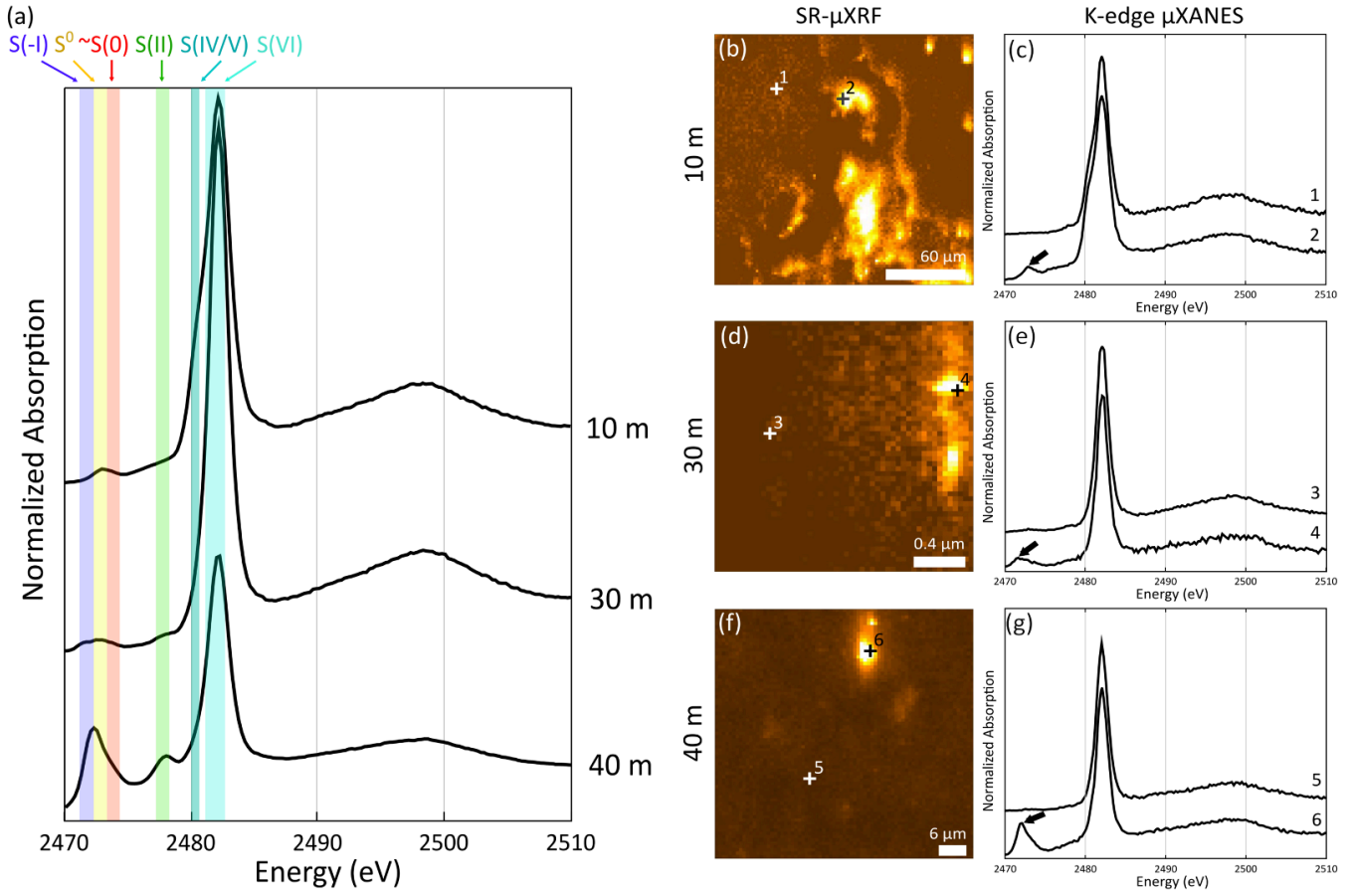

Figure 7. (a) S K-edge XANES spectra of Lake Alchichica microbialites (October 2022). Ranges of S oxidation states are highlighted by different lines with distinct colors: dark blue for S(-I), yellow for S^0, red for organic S(-I) to S(0.5), green for S(II), medium blue for S(IV) to S(V) and light blue for S(VI). At the top: Average S K-edge XANES spectrum (over 28 spectra) of the 10 m deep microbialite sample. In the middle: Average S K-edge XANES spectrum (over 37 spectra) of the 30 m deep microbialite sample. At the bottom: Average S K-edge XANES spectrum (over 23 spectra) of the 40 m deep microbialite sample. On the right: Spatial distribution of S in microbialites at different depths. SR-µXRF S maps of a mixed aragonite-hydromagnesite zone (see Fig. S6) are shown for the (b) 10 m deep, (d) 30 m deep and (f) 40 m deep microbialite samples. Crosses indicate the locations where S K-edge XANES spectra shown in (c), (e) and (g) were acquired. Spectra 1, 3 and 5 correspond to a diffuse S zone. Spectra 2, 4 and 6 correspond to a S hotspot. Arrows highlight a peak characteristic of a reduced S-species (S(-I) and/or S^0) in spectra 2, 4 and 6.

the average spectra of the k-means clusters C1 and C4; Fig. 10e-f).

Interestingly, SEM-EDXS analyses of the same region revealed that the reduced S-rich hotspots were spatially associated with rounded features (black edges in BSE) resembling aragonite-encrusted biogenic structures (Figs 10b, 11a). These hotspots also contained magnesium, silicon, and iron (Fig. 11b). Complementary SR-µXRF measurements on the same area showed that the reduced S hotspots were embedded within discrete P-rich laminae located in the aragonitic outer rim (Fig. 11e). Interestingly, these features were not directly observable within huntite.

4 Discussion

4.1 Origins of S in the water column and microbialites of Lake Alchichica

Lake Alchichica's water column contains approximately 11 mM of total dissolved S (this study; Alcocer, 2022; Muller et al., 2023), a relatively high concentration compared to that in most lacustrine systems (Zak et al., 2021). In modern lakes, S typically enters in the form of SO_4^{2-}. SO_4^{2-} could have multiple origins in Lake Alchichica: weathering of surrounding bedrock (from mineral SO_4^{2-} deposits or via FeS_2 oxidation), hydrolysis of organic matter in the water column, meteoric waters or aerosols inputs (Zak et al., 2021). Considering the volcanic nature of Alchichica's geological basement, a direct reduced S source to Lake Alchichica through volcanic outgassing cannot be excluded. Due to the wide range of S oxidation states exhibited by S species — from (-II) to (VI) — the S geochemical cycle is complex and likely involves several types of microbially-

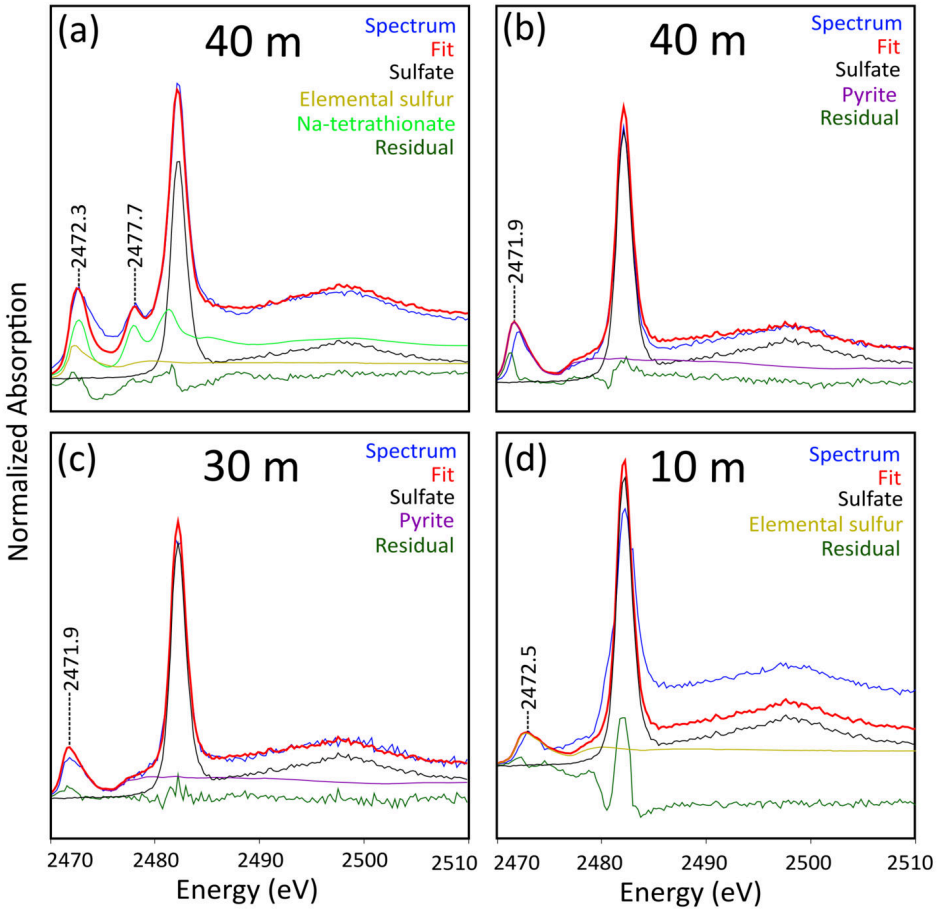

Figure 8. S K-edge μXANES spectra linear combination fitting. (a) Results of linear combination fitting for one S K-edge spectrum (red) of the 40 m deep sample using three reference compounds (internal reference for SO_4^{2-}, ID21, S^0 reference and Na-tetrathionate reference, with energy peaks at 2472.3 and 2477.7 eV). The residual is shown in green; (b) Linear combination fitting for another S K-edge spectrum (red) of the 40 m deep sample using two reference compounds (internal reference for SO_4^{2-} and the ID21 FeS_2 reference), showing the presence of FeS_2 (with energy peak at 2471.9 eV). The residual is shown in green. This spectrum is different from the one shown in (a), illustrating spatial variability within a single microbialite sample: the spectrum shown in (a) probed tetrathionate-like molecules, while the one shown in (b) probed pyrite instead. (c) Linear combination fitting for the 30 m deep sample S K-edge spectrum (red) using two reference compounds (internal reference for SO_4^{2-} and the ID21 FeS_2 (S(-I)) reference, suggesting the presence of FeS_2: with energy peak at 2471.9 eV). The residual is shown in green; (d) Linear combination fitting for the 10 m deep sample S K-edge spectrum (red) with two reference compounds (internal reference for SO_4^{2-} (S(VI)) and the ID21 S^0 reference), showing a good fit with S^0 (with energy peak at 2472.5 eV). The residual is shown in green.

catalyzed processes such as dissimilatory and assimilatory reductions, oxidation and disproportionation (Haglund et al., 2002; Lamers et al., 2002; Canfield et al., 2005b; Camacho, 2009; Luo et al., 2018). As a result, S in Alchichica microbialites may derive from (i) precipitation of dissolved SO_4^{2-} into carbonates, (ii) microbial S cycling in the water column and/or within microbialites, or (iii) a combination of both.

While our measurements did not allow us to assess the concentration of hydrogen sulfide throughout Lake Alchichica water column in May 2019 and October 2022, its presence was attested based on its smell in water samples collected below the oxycline at both times. Moreover, previous studies reported H_2S concentrations ranging from 0.08 to 0.13 mM in deep waters of Lake Alchichica during the stratification period (Hernández et al., 2014; Alcocer, 2022). Last, members of the *Thiomicrospiraceae*, a family of planktonic S-oxidizing chemolithoautotrophic Gammaproteobacteria, were abundant below the oxycline in October 2022, supporting the presence of dissolved sulfides (Alcocer, 2022; Iniesto et al., 2022) – as well as of other intermediate oxidized S compounds (including S^0). Overall, the seasonal development of anoxic conditions at the bottom of Lake Alchichica water column during summer and fall suggests that deep microbialites are seasonally exposed to various dissolved S compounds including sulfides.

4.2 Sulfates contained in Alchichica microbialites

Alchichica microbialites contain S, as clearly established by SEM-EDXS, S K-edge XANES, and XRF analyses. S, whether in oxidized or reduced form, presents a general phase-related distribution pattern: it is preferentially con-

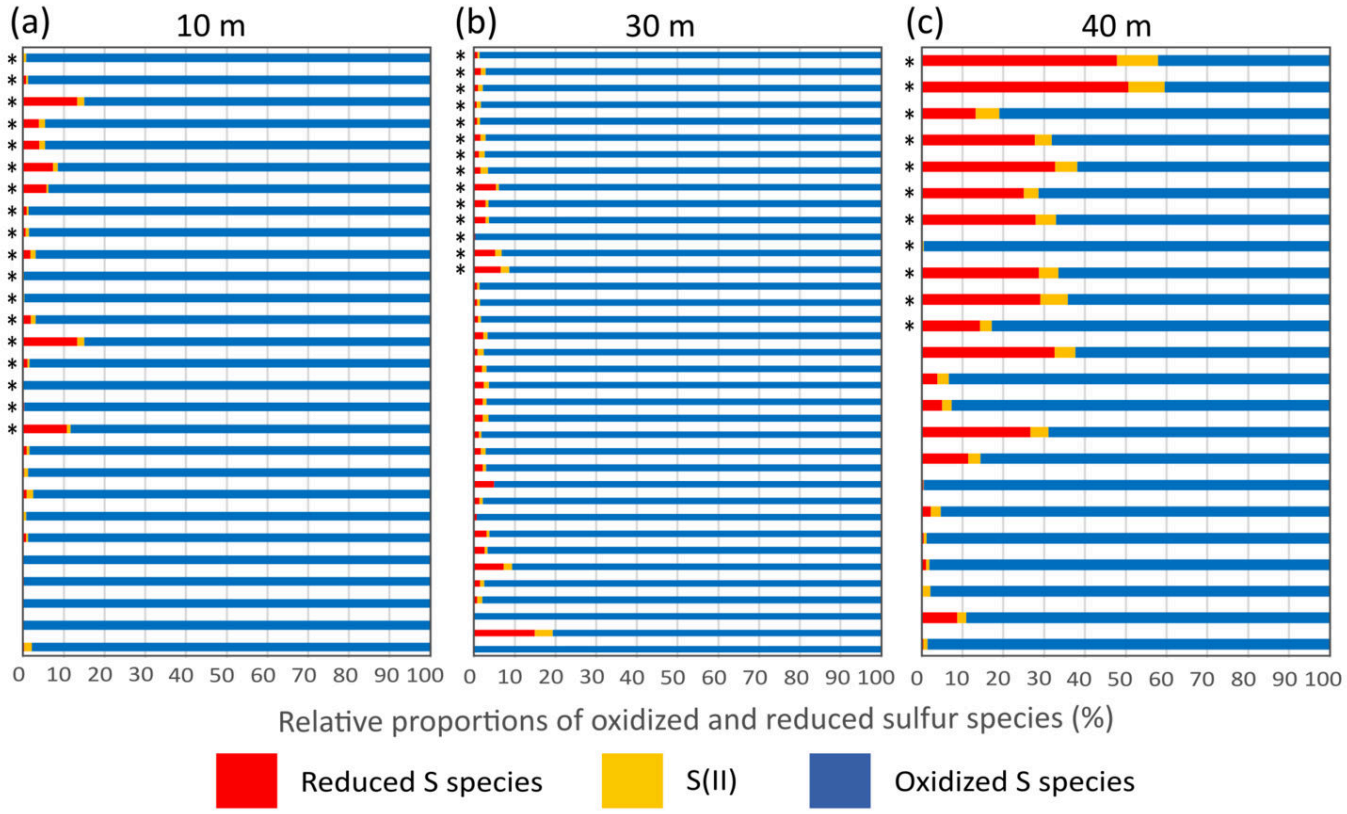

Figure 9. Relative quantification of three different S redox species (based on their respective energy ranges) in Lake Alchichica microbialites collected in October 2022. Each histogram bar corresponds to an individual acquired spectrum. The proportions of the spectral signals from reduced S species (from the energy range ~2471 to ~2473 eV), S(-I) to S^0, are in red; S(II) species (from ~2476 to ~2479 eV) are in yellow. Oxidized species, mainly SO_4^{2-} (S(VI) from ~2480 to ~2482 eV) are in blue. Spectra acquired in areas containing S hotspots have been marked with an asterisk. (a) Relative quantifications of S species in the 10 m deep sample; (b) Relative quantification of S species in the 30 m deep sample; (c) Relative quantification of S species in the 40 m deep sample.

centrated within the aragonite laminae of microbialites across all depths. By contrast, the S signal significantly weakens in deeper zones of the microbialites, dominated by hydromagnesite and/or huntite, even if it remains present, partly explaining some heterogeneities in the reduced S content within deep microbialite (Fig. 9). One possible explanation for this distribution pattern in microbialites is that S abundance is globally controlled by microbial activity. Supporting this hypothesis, aragonite typically forms the outer layers of the microbialites, where it entombs dense aggregates of cyanobacteria affiliated to the Pleurocapsales order (*Xenococcaceae* family in the Genome Taxonomy Database — GTDB-taxonomy: Parks et al., 2021; Couradeau et al., 2013; Gérard et al., 2013; Saghaï et al., 2015). Consequently, part of the detected S may originate from the degradation of organic S present within cyanobacterial cells, which is eventually oxidized into SO_4^{2-}. This is consistent with the overall low TOC of these samples showing intense carbon degradation (Havas et al., 2025). In contrast, no abundant cell remnants are observed in huntite- and hydromagnesite-rich areas.

An additional, non-exclusive explanation for this S distribution is that mineralogical factors influence S retention. S was predominantly identified as S(VI) across all microbialite samples, regardless of depth and irrespective of the carbonate mineral phases (aragonite, hydromagnesite or huntite), accounting for 40 % to 90 % of the total S K-edge XANES signal (Fig. S5). Comparison of the Alchichica microbialite diffuse S XANES spectra with reference compounds precludes the presence of calcium sulfate minerals, such as gypsum, since the distinctive features past the white line do not match (Fig. S7). These spectral features at ~2497 eV result from multiple scattering contributions from S species and are diagnostic of the mineral phase (Fleet, 2005; Veronesi et al., 2013). By contrast, the microbialite sulfate XANES spectra resemble those of (i) carbonate associated sulfates (CAS) and (ii) organosulfates.

The CAS hypothesis is plausible, although bulk FTIR analyses did not reveal CAS-specific spectral signatures. This may be due to the low amount of S in the microbialites, which may be below FTIR detection limits (Fig. S9). Yet, dissolved S concentrations remain elevated throughout the Lake Alchichica water column (~11 mM), supporting the possibility that SO_4^{2-} may be incorporated into precipitating carbonate phases, such as aragonite, through substitution of carbonate groups (Pingitore et al., 1995). Combined SR-μXRF and SEM observations show that at least a portion of the S is diffusely distributed and more abundant in aragonitic regions. This suggests that carbonate substitution by inorganic SO_4^{2-} may occur preferentially in aragonite rather

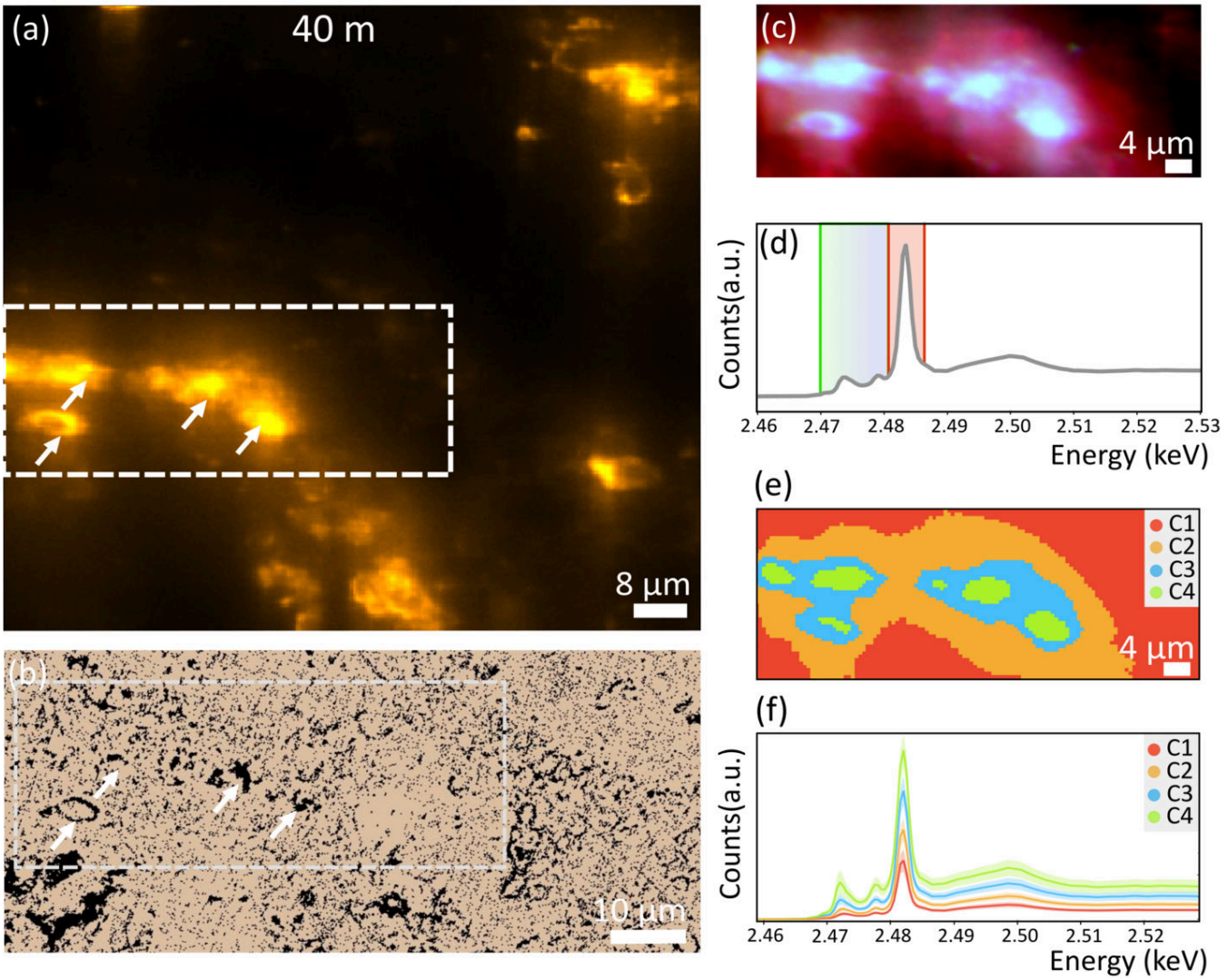

Figure 10. Hyperspectral map acquired on the 40 m deep microbialite (400 nm/pixel; 64 µm x 24 µm area). (a) SR-µXRF S map of an aragonitic layer within the 40 m deep microbialite thick section. The dashed rectangle indicates the area for the hyperspectral map. The arrows correspond to the object also highlighted by white arrows in the image (b); (b) BSE SEM image of the region highlighted in image (a). Note the 6–8 µm spherical shapes corresponding to biogenic structures in aragonite, outlined by black edges and marked with white arrows. Image contrast and color were modified using ImageJ software to highlight the edges of the biogenic remains. The dashed rectangle indicates the area for the hyperspectral map. (c) Cumulated S µXRF map integrated over excitation energies from 2471 to 2478 eV for the reduced and intermediate species (S(-I), S^0, S(II), shown in green to blue) and from 2478 to 2482 eV for the oxidized species (SO_4^{2-}, shown in red) in the zone highlighted in image (a). Circular objects are highlighted in this projection; (d) Average S K-edge XANES spectrum showing the energy range (in green-blue) for reduced and intermediate S species and (in red) for oxidized species; (e) k-means clustering of the S energy map from the zone highlighted in (a). Four clusters are used (C1, C2, C3, and C4), highlighting circular S-hotspots within a S-enriched area, and showing that these S hotspots contain a combination of oxidized and reduced S species, with reduced species being relatively more intense than in the surrounding area. (f) Mean S K-edge XANES spectra for the four clusters shown in (e), revealing characteristic reduced S peaks with increasing intensity toward the S hotspots. Each cluster is represented by an average spectrum and the envelopes around it correspond to the standard deviation.

than in huntite or hydromagnesite, potentially explaining the observed spatial distribution pattern (Figs 3, 9). We hypothesize that this preferential incorporation of SO_4^{2-} within aragonite could be attributed to (i) crystallographic factors that render the aragonite lattice more susceptible to SO_4^{2-} incorporation compared to huntite and hydromagnesite, or (ii) possible inhibitory effect of SO_4^{2-} on the precipitation or stability of huntite and hydromagnesite (Santos et al., 2024). These hypotheses will require further testing in the future, such as targeted analyses of the presence of CAS in Mg-carbonates and SO_4^{2-} incorporation kinetics within these phases. Alternatively, at least some of the sulfates in the microbialites could be in an organic form. Supporting this hypothesis, S XANES spectra from the Alchichica

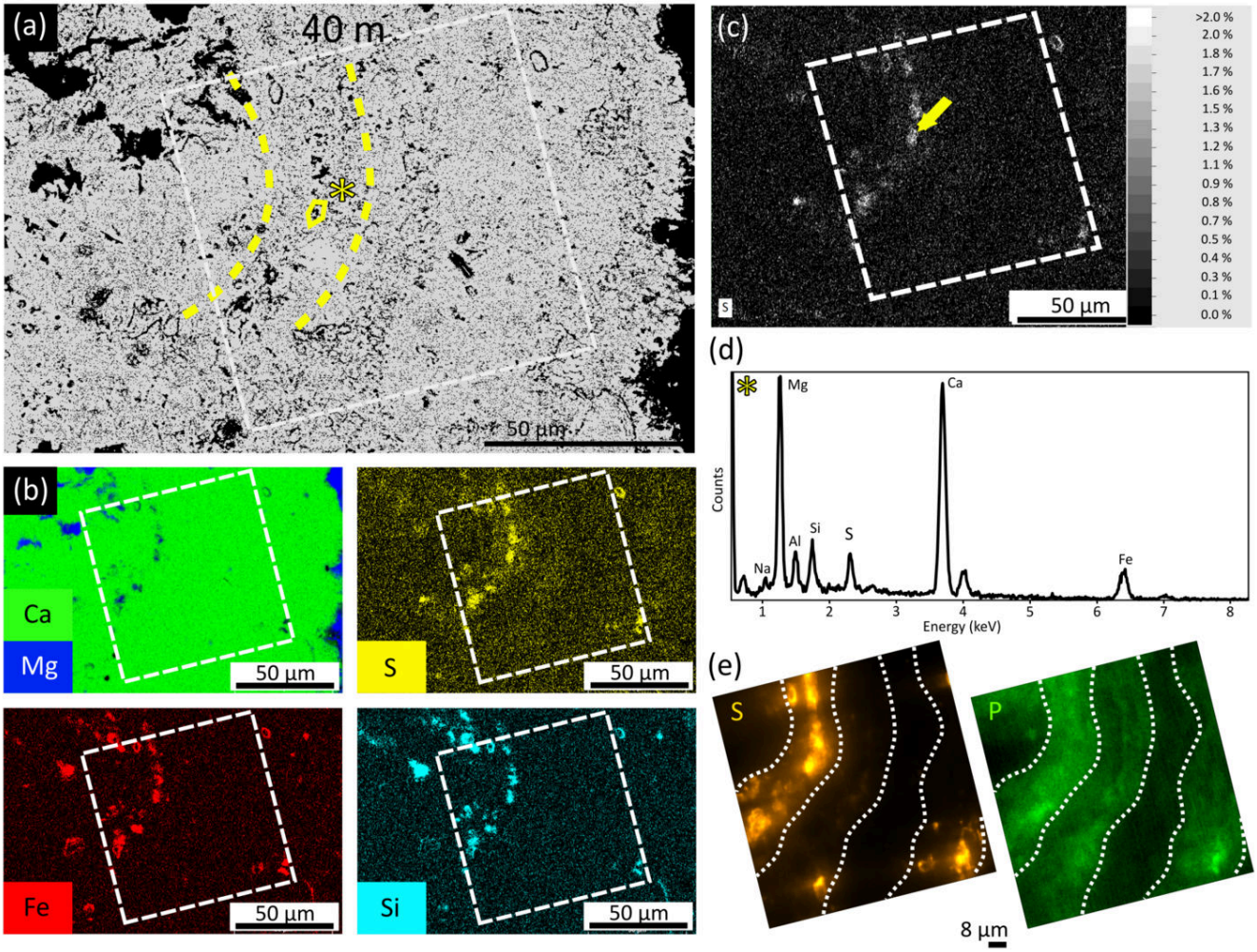

Figure 11. Association of silicon, magnesium and iron with S in an aragonitic layer of the Lake Alchichica microbialite collected in 2022. (a) BSE SEM image of an aragonitic layer from the 40 m deep sample, including the area marked with a white square where the SR-XRF map of Figure 10 with the biogenic S-enriched structures was acquired (white dashed square). Yellow dashed lines highlight the S-enriched laminae; (b) EDXS elemental map of calcium (green) and magnesium (blue) of image (a), showing aragonite and hydromagnesite zones, along with S (yellow), iron (red) and silica (turquoise) distributions; (c) Quantified map of S; (d) EDXS spectrum of S-enriched zones in image (a), indicated by the yellow arrow; (e) SR-µXRF S and phosphorus maps, acquired over the same zone as (a), showing S-enriched circular objects localized within phosphorus laminae, highlighted by dashed white lines.

microbialites closely resemble those of n-hexadecyl sulfate (taken as a model for organosulfates in general) as measured by Kajitani et al. (2023, Fig. S8). This similarity includes not only the main sulfate peak but also lower energy peaks at ~2473 and ~2477 eV.

Overall, the sulfates detected in the microbialites possibly represent a combination of organic sulfates and inorganic CAS. Future isotope analyses may enable us to better assess the organic vs inorganic origin of these sulfates, provided they display distinct isotopic compositions, and the transformation pathways through which they originate.

4.3 Anoxic conditions recorded by reduced S in microbialites

4.3.1 Detection of reduced S species in microbialites

Although the exact speciation of sulfate compounds in Alchichica microbialites, whether organic or inorganic, remains uncertain, reduced S species were undoubtedly detected in all of them (Fig. 7). Comparison with reference spectra from the literature suggests that part of this reduced S likely corresponds to organic S functions such as sulfoxides, polysulfides and/or heterocyclic S (cf. Orthous-Daunay et al., 2010, ID21 database; Fig. S6). Some of these species co-occurred as evidenced by spectral peaks at ~2472.9 eV (e.g. organic disulfides) and ~2477.7 eV (e.g. sulfoxides). In addition, both FeS_2 and S^0 were detected in Alchichica microbialites. Differentiating between these two compounds can be challenging due to overlapping peaks (Wang et al., 2015). However, subtle shifts in energy ranges were observed for these peaks, allowing us to assign peaks at ~2471.3–2472.2 eV to FeS_2 and those at ~2472.5–2472.9 eV to S^0. These reduced S species were mostly co-localized in hotspots of variable sizes and shapes, as attested by SR-µXRF and SEM-EDXS (Figs 6, 7), predominantly

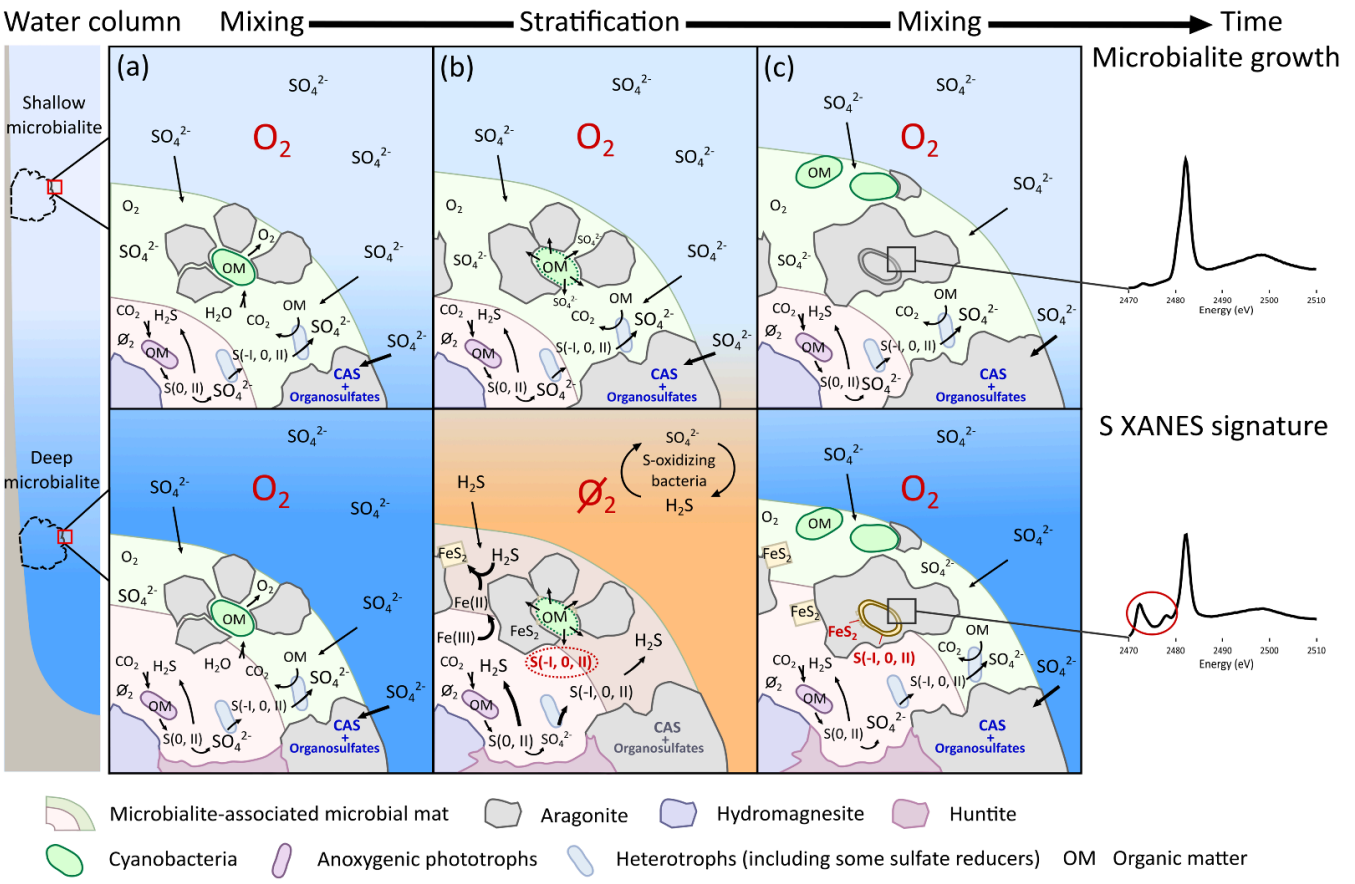

Figure 12. Schematic representation of S speciation recorded in shallow and deep microbialites during lake mixing and stratification. The following abbreviations are used: CAS for carbonate-associated sulfates; S(-I, 0, II) for reduced sulfur species. (a) During the lake's mixing period (oxic water column), some bacterial cells in both shallow and deep microbialites are encrusted by aragonite at the surface of microbialites. SO_4^{2-} from the water column and the microbial mat is actively processed and incorporated into microbialites as CAS and/or organosulfates. (b) During stratification, deep microbialites experience anoxia. Decay of bacterial cells in both shallow and deep microbialites releases S-containing organic matter into the encrusting microbial mat microenvironments. Microbial/redox production of reduced S species promotes FeS_2 precipitation. Sulfate-reducers and anoxygenic photoautotrophs metabolize S, which becomes stabilized under local reducing conditions and trapped within encrusting microbial mat around cell remnants. (c) When oxic conditions return, new bacterial cells are active and are encrusted by aragonite containing oxidized S species, while underlying aragonite layers in deep microbialites retain reduced S signatures (even in small amount) around cyanobacterial remnants, preserving evidence of past anoxic conditions. During early diagenesis, at least part of the primary aragonite and hydromagnesite is gradually replaced by diagenetic huntite at depth, which likely alters the cell remnants and associated S.

within aragonite-rich regions, although FeS_2 also occurred in hydromagnesite-dominated areas.

The presence of reduced S in microbialites, including those forming under continuously oxic conditions can be attributed to several mechanisms. (i) First, anoxygenic photosynthetic bacteria typically using hydrogen sulfide as an electron donor and producing S^0 are abundant in Alchichica microbialites. This indicates an active sulfur cycle within these ecosystems (Couradeau et al., 2011), which involves a diversity of reduced S species. (ii) Moreover, anoxic microzones often develop within microbialite-associated biofilms, even under globally oxygenated conditions. These microzones may favor the production of diverse reduced S species by photo- and chemolithoautotrophic microorganisms as well as sulfate-reducers (Pages et al., 2014; Vignale et al., 2025). These processes are further influenced at the local scale by diel cycles, which modulate shifts in the metabolic activity of oxygenic phototrophs (Pages et al., 2014). (iii) The preferential association of S with aragonite, which encrusts cells, suggests that at least some reduced S may originate from organic matter degradation, potentially accompanied by sulfurization reactions (Visscher et al., 2000; Schroth et al., 2007). (iv) Alternatively, microbial activity in sinking particulate matter within the deeper water column may also promote a sulfurization process, leading to the formation of sulfide-bound organic matter (Raven et al., 2021). This may, in turn, influence local geochemical cycles both in the vicinity of and within the microbialites.

4.3.2 Increase in reduced S content with depth and anoxia in microbialites

The relative abundance of reduced S species, including those associated with iron sulfides, increased with depth in Alchichica microbialites. For example, hotspots attributed to FeS_2, distributed across both aragonitic and hydromagnesite-dominated areas, became more pronounced in deeper samples, despite some variability. This was particularly evident in microbialites collected close to the oxycline in October 2022, at a depth of 30 m, where numerous FeS_2 occurrences were observed. This pattern is consistent with the hydrochemical data collected on the same date: at 30 m, the water column was anoxic, and a peak in dissolved iron concentration was detected just above. The dissolved iron might correspond to a reactive iron pool (dissolved and/or colloidal oxy(hydroxides)), which undergoes both microbial and abiotic transformations into iron sulfides below the oxycline (Canfield et al., 2005a; Nikeleit et al., 2025). Even though dissolved iron concentrations in the lake water column are low, seasonal stratification leading to deep-water anoxia can supply ferrous iron to microbialites. Under anoxic conditions, microbial reduction of Fe(III) may in addition occur within microbialite-associated micro-environments, where SO_4^{2-}-reducing bacteria could promote iron sulfide precipitation (Pages et al., 2014).

In parallel, XANES peaks corresponding to reduced S oxidation states between 0 and II, generally attributed to di-/polysulfides/sulfoxide functions in organic compounds, also intensified with depth. While sulfoxides can form due to beam-induced damage by electrons or X-rays (Castillo-Michel et al., 2016), this effect was considered minor here, given the consistent and depth-dependent increase of the relative abundance of these chemical species. Instead, this pattern suggests enhanced microbial S cycling at depth, potentially driven by an increased abundance and/or activity of S-metabolizing organisms, such as S-oxidizing bacteria, anoxygenic photosynthesizers using H_2S as an electron donor and sulfate reducers, all detected in surface microbialites in Alchichica (Saghaï et al., 2016). Supporting a primary microbial influence on S speciation, hotspots containing S^0 and sometimes sulfoxides functions were predominantly observed within aragonite-rich regions near biofilms in deep microbialites. Some of these hotspots displayed shapes and sizes consistent with encrusted bacteria and were located in phosphorus-rich laminae, which are likely enriched in organic matter at 40 m depth (Anderson et al., 2001). These observations suggest that reduced S species in Alchichica microbialites (including FeS_2, S^0, and organic S compounds) are associated with anaerobic microbial processes (Pages et al., 2014; Marin-Carbonne et al., 2022). These structures were not observed in huntite zones. This absence may be explained by the secondary formation of huntite during early diagenesis, which involves the destabilization (i.e. dissolution) of primary aragonite and hydromagnesite in the Mg-rich interstitial solutions of deep microbialites as recently demonstrated by Caumartin et al. (2025). This process likely degrades primary cell remnants and their S content. Interestingly, although huntite is thermodynamically the most stable phase under Lake Alchichica conditions, it is not a primary phase and its formation appeared to be kinetically hindered compared to the primary aragonite-hydromagnesite assemblage (Caumartin et al., 2025). Overall, this calls for more specific organic carbon mapping within these mineral phases (Couradeau et al., 2013). Such processes likely drove a dynamic S cycle within the water column and microbialite-associated biofilms, strongly modulated by seasonal redox fluctuations (Gomes et al., 2022; Marin-Carbonne et al., 2022). Upon re-oxygenation, sulfides, including Fe-S phases, are oxidized, releasing intermediate S species such as thiosulfates, polysulfides, or tetrathionate-like compounds, before eventually converting to their fully oxidized state i.e. SO_4^{2-} (Zopfi et al., 2004; Bao et al., 2022). These interpretations are summarized in Figure 12.

Overall, a clear distinction emerges between the S species in the shallow microbialites (where constant oxic conditions prevail in the water column) and those in deep microbialites (which experience seasonal anoxia). According to XANES spectra, this difference is primarily attributed to the presence of S^0, FeS_2 and organic S compounds at depth. As a result, and given that microbialite-associated biofilms rapidly respond to environmental changes, S speciation within microbialites may serve as an indicator of environments that experience anoxic conditions, at least seasonally. One possibility is that reduced S is incorporated into microbialites when no carbonate precipitation occurs, via sulfide formation within microbialite porosity. Alternatively, sulfides may be incorporated during microbialites growth (i.e. calcification), potentially when seasonal anoxic conditions prevail, while at the same time the lake water remains persistently supersaturated with respect to amorphous calcium carbonates and monohydrocalcite. In either scenario, S speciation suggests that deep microbialites record the water column redox stratification (Fig. 12).

An interesting unresolved question is how the diagenetic transformation of aragonite and hydromagnesite into huntite (Caumartin et al., 2025) influences S speciation. Future detailed investigations should focus on determining whether this mineralogical replacement, likely through dissolution and reprecipitation, leads to a reduction in the abundance of CAS on one hand (knowing that aragonite contains abundant CAS but hydromagnesite does not), and a loss of organic sulfur on the other hand, particularly given that aragonite often encrusts microbial cells.

5 Conclusion

In this study, we investigated S speciation in modern lacustrine microbialites from Lake Alchichica, comparing shallow microbialites, which experience constant oxic conditions with deep microbialites, which are exposed to seasonal anoxia. By combining bulk chemical analyses, laboratory XRF, SEM-EDXS, SR-μXRF and μXANES spectroscopy at the S K-edge, we demonstrate that S speciation varies with microbialite formation depth. While sulfate remains

the dominant S species at all depths, potentially present as a mixture of organic sulfate and CAS, a higher relative abundance of reduced S species, including FeS_2 and S^0, was observed in deep microbialites. This enrichment suggests that microbialites can record a redox-sensitive S signature, reflecting seasonal stratification and episodes of anoxia in the overlying water column. Moreover, our findings highlight the importance of multi-scale S speciation analyses to fully assess the redox history recorded in microbialites. While we clearly identify the redox stratification of the lake based on S speciation, the total S in the microbialites remains low and is mainly recorded as oxidized S at all depths. At Alchichica, this may be partly explained by the seasonal reoxidation of the entire lake water column, consistently with a TOC/TS ratio of around 5 in the samples (Berner and Raiswell, 1983). Finally, our findings reinforce the idea that microorganisms impact the local S cycle in microbialites. The S isotopic composition of FeS_2 has been proposed as a signature of microbial S cycling in past environments through the study of modern microbialites (Marin-Carbonne et al., 2022). We suggest that combining detailed S isotope and speciation analyses could be a powerful approach to reconstruct S cycling in ancient microbialites.

Acknowledgments

This project received financial support from the MITI interdisciplinary program of the CNRS and the French Agence Nationale de la Recherche (ANR) under grant Microbialite, ANR-18-CE02-0013-01. We thank the European Synchrotron Radiation Facility (ESRF) for providing access to synchrotron radiation facilities under the experiment reference number ES-1311. EK acknowledges funding from the European Union's Horizon 2020 research and innovation programme under the Marie Sklowdoska-Curie grant agreement No 101031812 'NanoBioS'. We also thank the IMPMC analytical platforms that enabled the data acquisition; Béatrice Doisneau, Stéphanie Delbrel and Imène Estève for the SEM-EDXS support, and the Laboratoire Géosciences Océan in Brest, France, for the XRF data acquisition. JC was supported by a doctoral fellowship from the "Interface pour le vivant" program at Sorbonne Université.

Data, code, and outputs availability

Data on synchrotron-based µXANES and µXRF, as well as data on bulk chemical analyses on microbialite samples used in this study are available in Caumartin and Benzerara (2026): https://doi.org/10.5281/zenodo.20261425. The Supplementary Material includes 7 figures. Main text figures are available for download in the online version of this article.

Competing interests

The authors declare no competing interests.

Licence agreement

References

Alcocer J (ed.) (2022). *Lake Alchichica Limnology: The Uniqueness of a Tropical Maar Lake*. Springer International Publishing. doi:10.1007/978-3-030-79096-7

Alcocer J, Lugo A (2003). Effects of El Niño on the dynamics of Lake Alchichica, central Mexico. *Geofísica Internacional* 42(3): 523–528. doi:10.22201/igeof.00167169p.2003.42.3.943

Alcántara-Hernández RJ, Macek M, Torres-Huesca J, Arellano-Posadas J, Valdespino-Castillo PM (2022). Bacterioplankton. In Alcocer J (ed.) *Lake Alchichica Limnology: The Uniqueness of a Tropical Maar Lake*, p. 183–196. Springer International Publishing. doi:10.1007/978-3-030-79096-7_11

Allwood AC, Walter MR, Kamber BS, Marshall CP, Burch IW (2006). Stromatolite reef from the Early Archaean era of Australia. *Nature* 441(7094): 714–718. doi:10.1038/nature04764

Anderson LD, Delaney ML, Faul KL (2001). Carbon to phosphorus ratios in sediments: Implications for nutrient cycling. *Global Biogeochemical Cycles* 15(1): 65–79. doi:10.1029/2000GB001270

Antunes G, Warren L, Okubo J, Fairchild T, Varejão F, Uhlein G, Inglez L, Poiré D, Bahniuk A, Simões M (2022). The rise and fall of the giant stromatolites of the Lower Permian Irati Formation (Paraná Basin, Brazil): A multi-proxy based paleoenvironmental reconstruction. *Palaeogeography, Palaeoclimatology, Palaeoecology* 606: 111246. doi:10.1016/j.palaeo.2022.111246

Assayag N, Rivé K, Ader M, Jézéquel D, Agrinier P (2006). Improved method for isotopic and quantitative analysis of dissolved inorganic carbon in natural water samples. *Rapid Communications in Mass Spectrometry* 20(15): 2243–2251. doi:10.1002/rcm.2585

Bao Z, Bain J, Saurette E, Zou Finfrock Y, Hu Y, Ptacek CJ, Blowes DW (2022). Mineralogy-dependent sulfide oxidation via polysulfide and thiosulfate pathways during weathering of mixed-sulfide bearing mine waste rock. *Geochimica et Cosmochimica Acta* 317: 523–537. doi:10.1016/j.gca.2021.10.012

Bautista-Reyes F, Macek M (2012). Ciliate food vacuole content and bacterial community composition in the warm-monomictic crater Lake Alchichica, México. *FEMS Microbiology Ecology* 79(1): 85–97. doi:10.1111/j.1574-6941.2011.01200.x

Berner RA, Raiswell R (1983). Burial of organic carbon and pyrite sulfur in sediments over phanerozoic time: a new theory. *Geochimica et Cosmochimica Acta* 47(5): 855–862. doi:10.1016/0016-7037(83)90151-5

Bosak T, Greene S, Newman D (2007). A likely role for anoxygenic photosynthetic microbes in the formation of ancient stromatolites. *Geobiology* 5(2): 119–126. doi:10.1111/j.1472-4669.2007.00104.x

Burne RV, Moore LS (1987). Microbialites: Organosedimentary Deposits of Benthic Microbial Communities. *PALAIOS* 2(3): 241–254. doi:10.2307/3514674

Camacho A (2009). Sulfur Bacteria. In *Encyclopedia of Inland Waters*, p. 261–278. Elsevier. doi:10.1016/b978-012370626-3.00128-9

Canfield D, Kristensen E, Thamdrup B (2005a). The Iron and Manganese Cycles. In Canfield D, Kristensen E, Thamdrup B (eds.) *Advances in Marine Biology, Aquatic Geomicrobiology*, p. 269–312. Academic Press. doi:10.1016/S0065-2881(05)48008-6

Canfield D, Kristensen E, Thamdrup B (2005b). The Sulfur Cycle. In Canfield D, Kristensen E, Thamdrup B (eds.) *Advances in Marine Biology, Aquatic Geomicrobiology*, p. 313–381. Academic Press. doi:10.1016/S0065-2881(05)48009-8

Castillo-Michel HA, Diaz-Sanchez AG, Martinez-Martinez A, Hesse B (2016). Investigations of Sulfur Chemical Status with Synchrotron Micro Focused X-ray fluorescence and X-ray Absorption Spectroscopy. *Protein & Peptide Letters* 23(3): 291–299. doi:10.2174/0929866523666160108120117

Caumartin J, Benzerara K (2026). Sulfur and phosphorus SR-µXANES and µXRF analyses, bulk mineralogical, laboratory XRF and SEM-EDXS data from carbonate microbialites in Lake Alchichica [Dataset]. Version v3. Zenodo. doi:10.5281/zenodo.20261425

Caumartin J, Benzerara K, Havas R, Thomazo C, Fogret L, Betancourt V, Tavera R, Doisneau B, Jézéquel D, López-García P (2025). Huntite [$CaMg_3(CO_3)_4$], a Rare Carbonate Phase Formed during Early Diagenesis in Modern Microbialites. *ACS Earth and Space Chemistry* 9(6): 1544–1565. doi:10.1021/acsearthspacechem.5c00022

Caumartin J, Benzerara K, Havas R, Thomazo C, Lòpez-García P, Duprat E (2023). The chemical conditions necessary for the formation of microbialites. *Geochemical Perspectives Letters* 25: 30–35. doi:10.7185/geochemlet.2311

Chako Tchamabé B, Carrasco-Núñez G, Miggins DP, Németh K (2020). Late Pleistocene to Holocene activity of Alchichica maar volcano, eastern Trans-Mexican Volcanic Belt. *Journal of South American Earth Sciences* 97: 102404. doi:10.1016/j.jsames.2019.102404

Couradeau E, Benzerara K, Gérard E, Estève I, Moreira D, Tavera R, López-García P (2013). Cyanobacterial calcification in modern microbialites at the submicrometer scale. *Biogeosciences* 10(8): 5255–5266. doi:10.5194/bg-10-5255-2013

Couradeau E, Benzerara K, Moreira D, Gérard E, Kaźmierczak J, Tavera R, López-García P (2011). Prokaryotic and Eukaryotic Community Structure in Field and Cultured Microbialites from the Alkaline Lake Alchichica (Mexico). *PLoS ONE* 6(12): e28767. doi:10.1371/journal.pone.0028767

Einsiedl F, Schäfer T, Northrup P (2007). Combined sulfur K-edge XANES spectroscopy and stable isotope analyses of fulvic acids and groundwater sulfate identify sulfur cycling in a karstic catchment area. *Chemical Geology* 238(3-4): 268–276. doi:10.1016/j.chemgeo.2006.11.014

Ferrari L, Orozco-Esquivel T, Manea V, Manea M (2012). The dynamic history of the Trans-Mexican Volcanic Belt and the Mexico subduction zone. *Tectonophysics* 522–523: 122–149. doi:10.1016/j.tecto.2011.09.018

Fleet ME (2005). XANES Spectroscopy of Sulfur in Earth Materials. *The Canadian Mineralogist* 43(6): 1811–1838. doi:10.2113/gscanmin.43.6.1811

Gomes ML, Klatt JM, Dick GJ, Grim SL, Rico KI, Medina M, Ziebis W, Kinsman-Costello L, Sheldon ND, Fike DA (2022). Sedimentary pyrite sulfur isotope compositions preserve signatures of the surface microbial mat environment in sediments underlying low-oxygen cyanobacterial mats. *Geobiology* 20(1): 60–78. doi:10.1111/gbi.12466

Gérard E, Ménez B, Couradeau E, Moreira D, Benzerara K, Tavera R, López-García P (2013). Specific carbonate–microbe interactions in the modern microbialites of Lake Alchichica (Mexico). *The ISME Journal* 7(10): 1997–2009. doi:10.1038/ismej.2013.81

Haglund AL, Törnblom E, Boström B, Tranvik L (2002). Large Differences in the Fraction of Active Bacteria in Plankton, Sediments, and Biofilm. *Microbial Ecology* 43(2): 232–241. doi:10.1007/s00248-002-2005-0

Hastie T, Tibshirani R, Friedman J (2009). Unsupervised Learning. In *The Elements of Statistical Learning*, p. 485–585. Springer New York. doi:10.1007/978-0-387-84858-7_14

Havas R, Thomazo C, Caumartin J, Iniesto M, Bert H, Jézéquel D, Moreira D, Tavera R, Bettencourt V, López-García P, Vennin E, Benzerara K (2025). Untangling the Primary Biotic and Abiotic Controls on Oxygen, Inorganic and Organic Carbon Isotope Signals in Modern Microbialites. *Geobiology* 23(1): 70012. doi:10.1111/gbi.70012

Havas R, Thomazo C, Iniesto M, Jézéquel D, Moreira D, Tavera R, Caumartin J, Muller E, López-García P, Benzerara K (2023). The hidden role of dissolved organic carbon in the biogeochemical cycle of carbon in modern redox-stratified lakes. *Biogeosciences* 20(12): 2405–2424. doi:10.5194/bg-20-2405-2023

Hernández MdC, Alcocer J, Oseguera LA, Escobar E (2014). Profundal benthic invertebrates in an oligotrophic tropical lake: different strategies for coping with anoxia. *Journal of Limnology* 73(2). doi:10.4081/jlimnol.2014.910

Hohl SV, Viehmann S (2021). Stromatolites as geochemical archives to reconstruct microbial habitats through deep time: Potential and pitfalls of novel radiogenic and stable isotope systems. *Earth-Science Reviews* 218: 103683. doi:10.1016/j.earscirev.2021.103683

Iniesto M, Moreira D, Benzerara K, Reboul G, Bertolino P, Tavera R, López-García P (2022). Planktonic microbial communities from microbialite-bearing lakes sampled along a salinity-alkalinity gradient. *Limnology and Oceanography* 67(12): 2718–2733. doi:10.1002/lno.12233

Iniesto M, Moreira D, Reboul G, Deschamps P, Benzerara K, Bertolino P, Saghaï A, Tavera R, López-García P (2021). Core microbial communities of lacustrine microbialites sampled along an alkalinity gradient. *Environmental Microbiology* 23(1): 51–68. doi:10.1111/1462-2920.15252

Kajitani I, Koike M, Nakada R, Tanabe G, Usui T, Matsu'ura F, Fukushi K, Yokoyama T (2023). Identification of carbonate-associated sulfate (CAS) in a Noachian Martian meteorite Allan Hills 84001. *Earth and Planetary Science Letters* 620: 118345. doi:10.1016/j.epsl.2023.118345

Kaźmierczak J, Kempe S, Kremer B, López-García P, Moreira D, Tavera R (2011). Hydrochemistry and microbialites of the alkaline crater lake Alchichica, Mexico. *Facies* 57(4): 543–570. doi:10.1007/s10347-010-0255-8

Lamers LPM, Falla S, Samborska EM, Dulken IARv, Hengstum Gv, Roelofs JGM (2002). Factors controlling the extent of eutrophication and toxicity in sulfate-polluted freshwater wetlands. *Limnology and Oceanography* 47(2): 585–593. doi:10.4319/lo.2002.47.2.0585

Luo G, Richoz S, van de Schootbrugge B, Algeo TJ, Xie S, Ono S, Summons RE (2018). Multiple sulfur-isotopic evidence for a shallowly stratified ocean following the Triassic-Jurassic boundary mass extinction. *Geochimica et Cosmochimica Acta* 231: 73–87. doi:10.1016/j.gca.2018.04.015

Marin-Carbonne J, Decraene MN, Havas R, Remusat L, Pasquier V, Alléon J, Zeyen N, Bouton A, Bernard S, Escrig S, Olivier N, Vennin E, Meibom A, Benzerara K, Thomazo C (2022). Early precipitated micropyrite in microbialites: A time capsule of microbial sulfur cycling. *Geochemical Perspectives Letters* 21: 7–12. doi:10.7185/geochemlet.2209

Muller E, Rapin W, Caumartin J, Jézéquel D, De Wever A, Thomazo C, Havas R, López-García P, Moreira D, Tavera R, Benzerara K (2023). Diagenetic formation of stevensite by replacement of diatom frustules in the sediments of the alkaline Lake Alchichica (Mexico). *Sedimentology* 70(4): 1013–1038. doi:10.1111/sed.13069

Myneni SCB (2000). X-Ray and Vibrational Spectroscopy of Sulfate in Earth Materials. *Reviews in Mineralogy and Geochemistry* 40(1): 113–172. doi:10.2138/rmg.2000.40.2

Nikeleit V, Maisch M, Straub D, Eroglu S, Lopez-Rivoldi JC, Strauss H, Ring-Hrubesh F, Byrne JM, Kappler A, Bryce C (2025). Cryptic iron cycling influenced by organic carbon availability in a seasonally stratified lake. *FEMS Microbiology Ecology* 101(4): 029. doi:10.1093/femsec/fiaf029

Ollivier B, Zeyen N, Gales G, Hickman-Lewis K, Gaboyer F, Benzerara K, Westall F (2018). Importance of Prokaryotes in the Functioning and Evolution of the Present and Past Geosphere and Biosphere. In *Prokaryotes and Evolution*, p. 57–129. Springer International Publishing. doi:10.1007/978-3-319-99784-1_3

Orthous-Daunay FR, Quirico E, Lemelle L, Beck P, deAndrade V, Simionovici A, Derenne S (2010). Speciation of sulfur in the insoluble organic matter from carbonaceous chondrites by XANES spectroscopy. *Earth and Planetary Science Letters* 300(3-4): 321–328. doi:10.1016/j.epsl.2010.10.012

Pages A, Welsh DT, Teasdale PR, Grice K, Vacher M, Bennett WW, Visscher PT (2014). Diel fluctuations in solute distributions and biogeochemical cycling in a hypersaline microbial mat from Shark Bay, WA. *Marine Chemistry* 167: 102–112. doi:10.1016/j.marchem.2014.05.003

Parks DH, Chuvochina M, Rinke C, Mussig AJ, Chaumeil PA, Hugenholtz P (2021). GTDB: an ongoing census of bacterial and archaeal diversity through a phylogenetically consistent, rank normalized and complete genome-based taxonomy. *Nucleic Acids Research* 50(D1): D785–D794. doi:10.1093/nar/gkab776

Pingitore NE, Meitzner G, Love KM (1995). Identification of sulfate in natural carbonates by x-ray absorption spectroscopy. *Geochimica et Cosmochimica Acta* 59(12): 2477–2483. doi:10.1016/0016-7037(95)00142-5

Pouchou JL, Pichoir F (1991). Quantitative Analysis of Homogeneous or Stratified Microvolumes Applying the Model "PAP". In Heinrich K, Newbury D (eds.) *Electron Probe Quantitation*, p. 31–75. Springer US, Boston, MA. doi:10.1007/978-1-4899-2617-3_4

Prietzel J, Tyufekchieva N, Eusterhues K, Kögel-Knabner I, Thieme J, Paterson D, McNulty I, de Jonge M, Eichert D, Salomé M (2009). Anoxic versus oxic sample pretreatment: Effects on the speciation of sulfur and iron in well-aerated and wetland soils as assessed by X-ray absorption near-edge spectroscopy (XANES). *Geoderma* 153(3-4): 318–330. doi:10.1016/j.geoderma.2009.08.015

Raven MR, Keil RG, Webb SM (2021). Rapid, Concurrent Formation of Organic Sulfur and Iron Sulfides During Experimental Sulfurization of Sinking Marine Particles. *Global Biogeochemical Cycles* 35(9): 2021 007062. doi:10.1029/2021GB007062

Saghaï A, Zivanovic Y, Moreira D, Benzerara K, Bertolino P, Ragon M, Tavera R, López-Archilla AI, López-García P (2016). Comparative metagenomics unveils functions and genome features of microbialite-associated communities along a depth gradient. *Environmental Microbiology* 18(12): 4990–5004. doi:10.1111/1462-2920.13456

Saghaï A, Zivanovic Y, Zeyen N, Moreira D, Benzerara K, Deschamps P, Bertolino P, Ragon M, Tavera R, López-Archilla AI, López-García P (2015). Metagenome-based diversity analyses suggest a significant contribution of non-cyanobacterial lineages to carbonate precipitation in modern microbialites. *Frontiers in Microbiology* 6. doi:10.3389/fmicb.2015.00797

Santos HS, Nguyen H, Illikainen S, Alzeer MIM, Cunha S, Kinnunen P (2024). Effect of Ammonium Sulfate on the Precipitation Mechanism of Mg Carbonates. *Crystal Growth & Design* 24(17): 7044–7058. doi:10.1021/acs.cgd.4c00700

Sarret G, Connan J, Kasrai M, Bancroft G, Charrié-Duhaut A, Lemoine S, Adam P, Albrecht P, Eybert-Bérard L (1999). Chemical forms of sulfur in geological and archeological asphaltenes from Middle East, France, and Spain determined by sulfur K- and L-edge X-ray absorption near-edge structure spectroscopy. *Geochimica et Cosmochimica Acta* 63(22): 3767–3779. doi:10.1016/S0016-7037(99)00205-7

Schroth AW, Bostick BC, Graham M, Kaste JM, Mitchell MJ, Friedland AJ (2007). Sulfur species behavior in soil organic matter during decomposition. *Journal of Geophysical Research: Biogeosciences* 112(G4). doi:10.1029/2007JG000538

Shih PM, Hemp J, Ward LM, Matzke NJ, Fischer WW (2016). Crown group Oxyphotobacteria postdate the rise of oxygen. *Geobiology* 15(1): 19–29. doi:10.1111/gbi.12200

Solé V, Papillon E, Cotte M, Walter P, Susini J (2007). A multiplatform code for the analysis of energy-dispersive X-ray fluorescence spectra. *Spectrochimica Acta Part B: Atomic Spectroscopy* 62(1): 63–68. doi:10.1016/j.sab.2006.12.002

Sánchez Medina X, Macek M, Bautista-Reyes F, Perz A, Bonilla Lemus P, Chávez Arteaga M (2016). Inter-annual ciliate distribution variation within the late stratification oxycline in a monomictic lake, Lake Alchichica (Mexico). *Journal of Limnology* 75(s1). doi:10.4081/jlimnol.2016.1440

Toplak M, Read ST, Sandt C, Borondics F (2021). Quasar: Easy Machine Learning for Biospectroscopy. *Cells* 10(9): 2300. doi:10.3390/cells10092300

Valdespino-Castillo PM, Alcántara-Hernández RJ, Alcocer J, Merino-Ibarra M, Macek M, Falcón LI (2014). Alkaline phosphatases in microbialites and bacterioplankton from Alchichica soda lake, Mexico. *FEMS Microbiology Ecology* 90: 504–519. doi:10.1111/1574-6941.12411

Veronesi G, Koudouna E, Cotte M, Martin FL, Quantock AJ (2013). X-ray absorption near-edge structure (XANES) spectroscopy identifies differential sulfur speciation in corneal tissue. *Analytical and Bioanalytical Chemistry* 405(21): 6613–6620. doi:10.1007/s00216-013-7120-x

Vignale FA, Sánchez-García L, Carrizo D, Castillejos Sepúlveda A, Taubner H, Oriolo S, Mitchell AL, Turjanski AG, Klatt JM, Finn RD, Garcia-Alai MM, Farías ME (2025). Seasonal biogeochemical variations in a modern microbialite reef under early Earth-like conditions. *Communications Earth & Environment* 6(1): 751. doi:10.1038/s43247-025-02764-6

Vilaclara G, Oliva-Martínez MG, Macek M, Ortega-Mayagoitia E, Alcántara-Hernández RJ, López-Vázquez C (2022). Phytoplankton of Alchichica: A Unique Community for an Oligotrophic Lake. In *Lake Alchichica Limnology*, p. 197–211. Springer International Publishing. doi:10.1007/978-3-030-79096-7_12

Visscher PT, Gallagher KL, Bouton A, Farias ME, Kurth D, Sancho-Tomás M, Philippot P, Somogyi A, Medjoubi K, Vennin E, Bourillot R, Walter MR, Burns BP, Contreras M, Dupraz C (2020). Modern arsenotrophic microbial mats provide an analogue for life in the anoxic Archean. *Communications Earth & Environment* 1(1): 1–10. doi:10.1038/s43247-020-00025-2

Visscher PT, Pamela Reid R, Bebout BM (2000). Microscale observations of sulfate reduction: Correlation of microbial activity with lithified micritic laminae in modern marine stromatolites. *Geology* 28(10): 919. doi:10.1130/0091-7613(2000)28<919:moosrc>2.0.co;2

Vogt LI, Cotelesage JJH, Dolgova NV, Boyes C, Qureshi M, Sokaras D, Sharifi S, George SJ, Pickering IJ, George GN (2023). Sulfur X-ray Absorption and Emission Spectroscopy of Organic Sulfones. *The Journal of Physical Chemistry A* 127(16): 3692–3704. doi:10.1021/acs.jpca.2c08647

Walter MR, Buick R, Dunlop JSR (1980). Stromatolites 3,400–3,500 Myr old from the North Pole area, Western Australia. *Nature* 284(5755): 443–445. doi:10.1038/284443a0

Wang P, Menzies NW, Lombi E, McKenna BA, James S, Tang C, Kopittke PM (2015). Synchrotron-based X-ray absorption near-edge spectroscopy imaging for laterally resolved speciation of selenium in fresh roots and leaves of wheat and rice. *Journal of Experimental Botany* 66(15): 4795–4806. doi:10.1093/jxb/erv254

Wiltfong R, Mitra-Kirtley S, Mullins OC, Andrews B, Fujisawa G, Larsen JW (2005). Sulfur Speciation in Different Kerogens by XANES Spectroscopy. *Energy & Fuels* 19(5): 1971–1976. doi:10.1021/ef049753n

Zak D, Hupfer M, Cabezas A, Jurasinski G, Audet J, Kleeberg A, McInnes R, Kristiansen SM, Petersen RJ, Liu H, Goldhammer T (2021). Sulphate in freshwater ecosystems: A review of sources, biogeochemical cycles, ecotoxicological effects and bioremediation. *Earth-Science Reviews* 212: 103446. doi:10.1016/j.earscirev.2020.103446

Zeyen N, Benzerara K, Beyssac O, Daval D, Muller E, Thomazo C, Tavera R, López-García P, Moreira D, Duprat E (2021). Integrative analysis of the mineralogical and chemical composition of modern microbialites from ten Mexican lakes: What do we learn about their formation? *Geochimica et Cosmochimica Acta* 305: 148–184. doi:10.1016/j.gca.2021.04.030

Zeyen N, Benzerara K, Menguy N, Brest J, Templeton AS, Webb SM, Gérard E, Moreira D, López-García P, Tavera R, Morin G (2019). Fe-bearing phases in modern lacustrine microbialites from Mexico. *Geochimica et Cosmochimica Acta* 253: 201–230. doi:10.1016/j.gca.2019.03.021

Zeyen N, Daval D, Lopez-Garcia P, Moreira D, Gaillardet J, Benzerara K (2017). Geochemical Conditions Allowing the Formation of Modern Lacustrine Microbialites. *Procedia Earth and Planetary Science* 17: 380–383. doi:10.1016/j.proeps.2016.12.096

Zopfi J, Ferdelman T, Fossing H (2004). Distribution and fate of sulfur intermediates—sulfite, tetrathionate, thiosulfate, and elemental sulfur—in marine sediments. In TW (ed.) *Sulfur Biogeochemistry - Past and Present*. Geological Society of America, J.P., Edwards, K.J., Lyons. doi:10.1130/0-8137-2379-5.97